Synthesis of New Magnetic Nanocomposite Materials for Data Storage

by

Haleema Alamri

A thesis
presented to the University of Waterloo
in fulfillment of the
thesis requirement for the degree of
Master of Science
in
Chemistry - Nanotechnology

Waterloo, Ontario, Canada, 2012

Declaration

I hereby declare that I am the sole author of this thesis. This is a true copy of the thesis, including any required final revisions, as accepted by my examiners.

I understand that my thesis may be made electronically available to the public.

Abstract

The confinement of magnetic nanoparticles (Prussian blue analogues (PBAs) has been achieved using mesostructured silica as a matrix. The PBAs have the general formula $A_xM_y[M'(CN)_n]_z$, where A is an alkali metal cation; M: Co^{II}, Ni^{II}, Sm^{III}; and M': Co^{II}. The two reactions were run in parallel and led to a mesostructured silica matrix that contains nanoparticles of PBA homogeneously distributed within the silica framework. As initially reported for the synthesis of $Co_3[Fe(CN)_6]_2$ magnetic nanoparticles, in the research conducted for this thesis, this synthesis has been extended to other compounds and to lanthanides such as Sm and has also included the study of the influence of different parameters (pH, concentration). As these nanocomposites are potentially good candidates for the preparation of bimetallic nanoparticles and oxides through controlled thermal treatment, the second goal of the research was to employ an adapted thermal treatment in order to prepare metal and metal oxide nanoparticles from PBA, directly embedded in the silica matrix. To this end, the influence of the thermal treatment (temperature, time, atmosphere) on the nature and structure of the resulting materials was investigated, with a focus on the potential use of the combustion of the organic templates as in-situ reducing agents. For some compounds, the preparation of bimetallic nanoparticles was successful. This method was tentatively applied to the preparation of specific Sm:Co bimetallic compounds, are well known as one of the best permanent magnets currently available.

Acknowledgements

I would to thank my supervisor, Prof.Eric Prouzet, for his encouragement, guidance and for his invaluable assistance during this work.

I would also like to thank my committee members Prof. Holger Kleinke, and Prof. Pavle Radovanovic.

I owe special thanks to my husband, Fawwaz, who accompanied me throughout this trip,and whose love, encouragements, and support helped me complete my study and overcome many problems, I also owe a great thanks to my wonderful children Abdulmalik and Eylan.

I also would like to thank my parents who I owe them more thanks than I can ever put into words. Special thanks also to all my graduate friends.

Financial support from Ministry of Higher Education In Saudi Arabia is appreciated.

Table of Contents

List of Figures

List of Tables

List of Abbreviations

Brij 98	$(C_{18}H_{35}(OCH_2CH_2)_{\sim 20}OH)$
emu.g^{-1}	Electromagnetic units per gram
FTIR	Fourier transform infrared spectroscopy
H_c	Coercive field
HMC	Hybrid micelle concentration
K	Kelvin
M_r	Remanent magnetization
M_s	Magnetization
Oe	Oersted
PBA	Prussian Blue Analogues
PBAs NPs	Prussian Blue Analogues Nano-particles
PEO	Poly(ethylene oxide), (PEO = (CH_2CH_2O))
PPMS	Physical property measurement system
SAXS	Small Angle X-ray Scattering
SEM	Scanning Electron Microscopy
SQUID	Superconducting Quantum Interference Device
TEM	Transmission Electron Microscopy
TEOS	Tetraethoxysilane (TEOS = $Si(OCH_2CH_3)_4$)
TP-XRD	Temperature-programmed X-ray diffraction
W	Watts
XRD	X-ray Powder Diffraction

Chapter 1

Introduction

1.1 Magnetism

Magnetism is the area of science that describes the magnetic behaviour of materials as a function of the application of an external magnetic field. Magnetization phenomena are the result of two causes: the magnetic moment due to the spin of electrons and the orbital motion of electrons.

All materials exhibit a diamagnetic component as a result of paired electrons, but some, if they possess unpaired electrons, exhibit an additional behaviour when exposed to a magnetic field, such as transition metal elements and lanthanides, which have unpaired electrons in the d and f orbitals.

The unpaired electron spins of an atom can interact with those of the other atoms and form spin alignments due to the atomic interaction of magnetic moments (Figure 1). If no interaction exists between the atomic magnetic moments, the material is said to be paramagnetic. This type of material shows only a small amount of magnetization in the presence of an external magnetic field, with the spin orientation being temperature dependent. On the other hand, in the presence of an interaction between atomic magnetic moments, magnetic behaviour that differs from paramagnetic can be observed; this behaviour is dependent mainly on the alignment of the spins. A parallel alignment produces ferromagnetic behaviour, and the material shows spontaneous magnetization below a given temperature, called the Curie temperature. Under the influence of an external magnetic field, ferromagnetic materials reach a saturated state. If the two magnetic

sub-networks are equal, an antiparallel alignment of spins creates antiferromagnetic compounds that exhibit no macroscopic magnetic properties. If the sub-networks differ, the material is said to be ferrimagnetic and shows a net magnetic moment.[1]

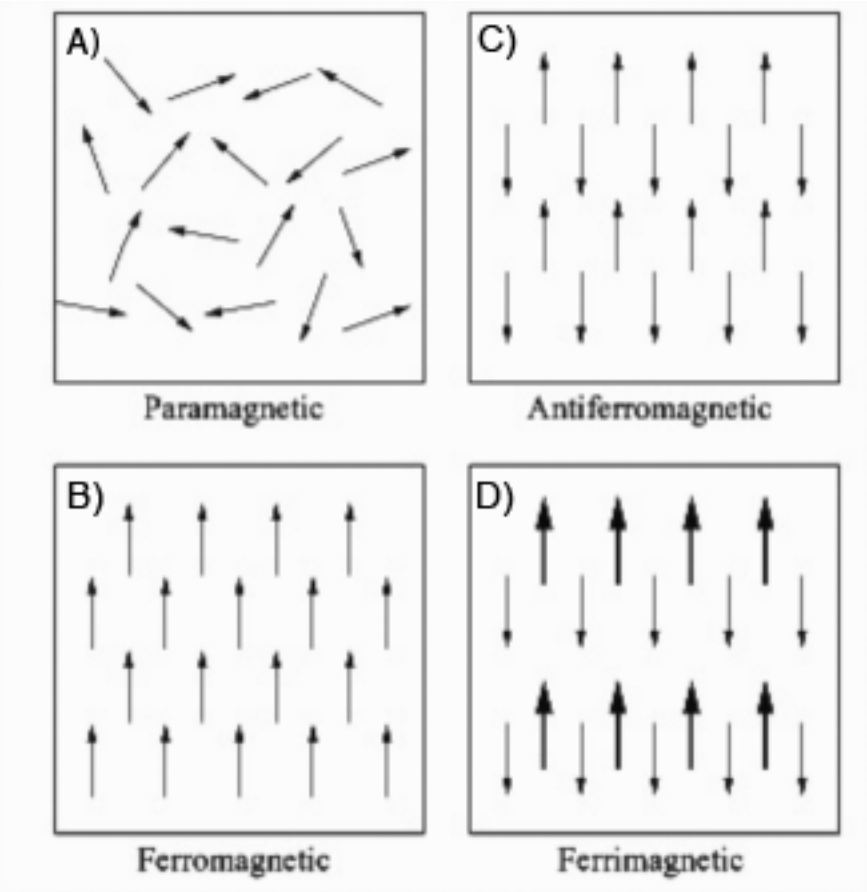

Figure 1. Different types of magnetism based on spin orientation under the influence of an external magnetic field: (A) Paramagnetic behaviour, in which the magnetic moments are equal but with random orientation; (B) Ferromagnetic behaviour, in which the magnetic moments are equal and parallel; (C) Antiferromagnetic behaviour, in which the magnetic moments are equal and antiparallel; (D) Ferrimagnetic behaviour, in which the magnetic moments are unequal and antiparallel. [1]

Generally, if a substance is placed in a magnetic field H, its magnetization M, is proportional to this magnetic field:

$$M = \chi H \tag{1}$$

where χ is the magnetic susceptibility (unit-less) and is a characteristic parameter of a particular material. A susceptibility value can be described as the measure of the response of a sample placed in an external magnetic field, and it is therefore a good indication of the magnetic behaviour of a material.[1]

The magnetic susceptibility of diamagnetic compounds has a small negative value, whereas paramagnetic and antiferromagnetic materials are associated with a small positive value of susceptibility (Figure 2). However, the magnitude of these values, as well as their temperature dependence, can help in distinguishing between those types of substances. Ferromagnetic substances, with a large positive susceptibility,[2] are especially interesting for scientists and engineers because those compounds can be used as a means of fabricating and developing magnetic data storage devices.[3]

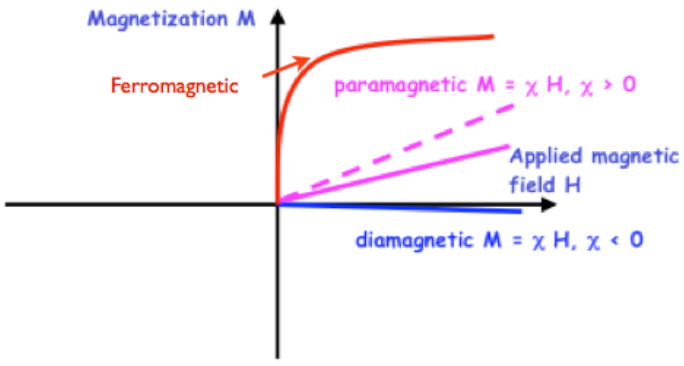

Figure 2. The variation in susceptibility of diamagnetic, paramagnetic, and ferromagnetic substances in a magnetic field.[4]

The application of a magnetic field causes the spins to align themselves with the external magnetic field. This effect appears as a gradual increase in the hysteresis loop as it approaches the saturation magnetization M_s Decreasing the intensity of the magnetic field causes some spins to become randomly oriented, which decreases the magnetization. When the magnetic field intensity drops to zero, ferromagnetic materials retain some magnetization, known as remanent magnetization, M_r. The intensity of the applied magnetic field in the negative direction that is needed in order to bring the magnetization back to zero is called the coercive field H_c (Figure 3).

The coercive field is a good indication of ferromagnetic resistance to becoming demagnetized. Hard ferromagnets are those with high coercivity, which enables them to be used as permanent magnets.[1]

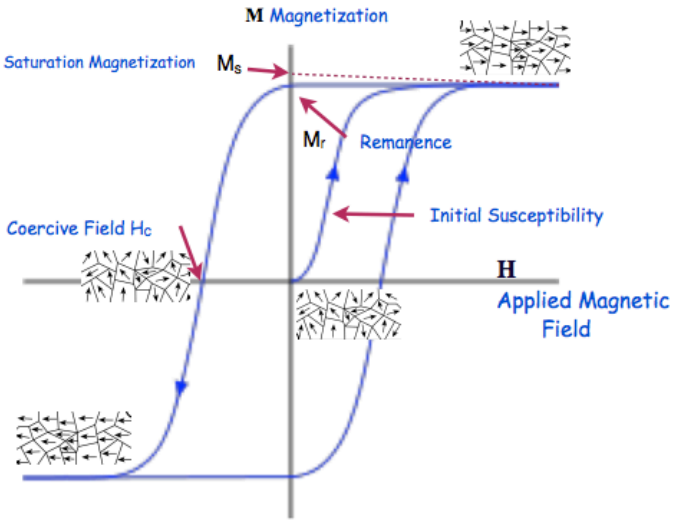

Figure 3. Important parameters (M_s, M_r, and H_c) that can be deduced from a hysteresis loop.[4]

1.2 Nanostructured Materials and Nanomagnetism

The alignment of magnetic moments within a crystalline structure extends only within a limited range. Bulk materials have particles with dimensions larger than the size of these magnetic domains, which means that each particle contains several magnetic domains separated by domain walls, which can be randomly oriented. These domain walls have characteristic thickness and energy associated with their formation and existence. Each domain is considered to be fully saturated. However, the random orientation of these domains prevents the bulk materials from exhibiting a final net magnetization, because different directions for those domains cancel the overall magnetization. When a magnetic field is applied, these domains orient themselves so that they align along the direction of the external magnetic field, which results in saturation magnetization. If the external magnetic field decreases, some remanent magnetization remains as a result of the stability of the domain walls, which can be cancelled only after the external magnetic field is reversed. The opposite magnetic field required for canceling the remanent magnetization is named the coercive magnetic field. This remanent magnetization depends on the stability of the domain walls so that both the remanent magnetization and coercive fields are good indicators of the magnetic properties of materials, especially with respect to their use for data storage. Indeed, high values for remanent magnetization and coercive fields are desirable because those values mean that the materials can retain the stored data for a long time and keep them intact under normal conditions. The ability to erase and rewrite data implies that the magnetization can be cancelled by means of a rather simple process. Potential candidates for magnetic storage must therefore exhibit optimal magnetic stability.

Demagnetization results from the rotation of domain walls, which is a simple process that requires little energy. Particles thus lose their magnetization under a relatively low magnetic field, and this magnetic field can be produced by other domains, leading to progressive demagnetization as a result of the interactions between magnetic domains. Researchers have solved this problem by reducing the particle size to values for which only one magnetic domain can appear within the particle, hence shifting from bulk to nanoscale. Nanostructured materials thus have useful properties that make them perfect candidates for data storage devices. As a result, since a single particle contains only one magnetic domain, it is assumed to contain only one bit of information. Therefore, reducing the size of the nanoparticles allows an increase both the density and the "quality" of information that can be stored per unit of surface area.

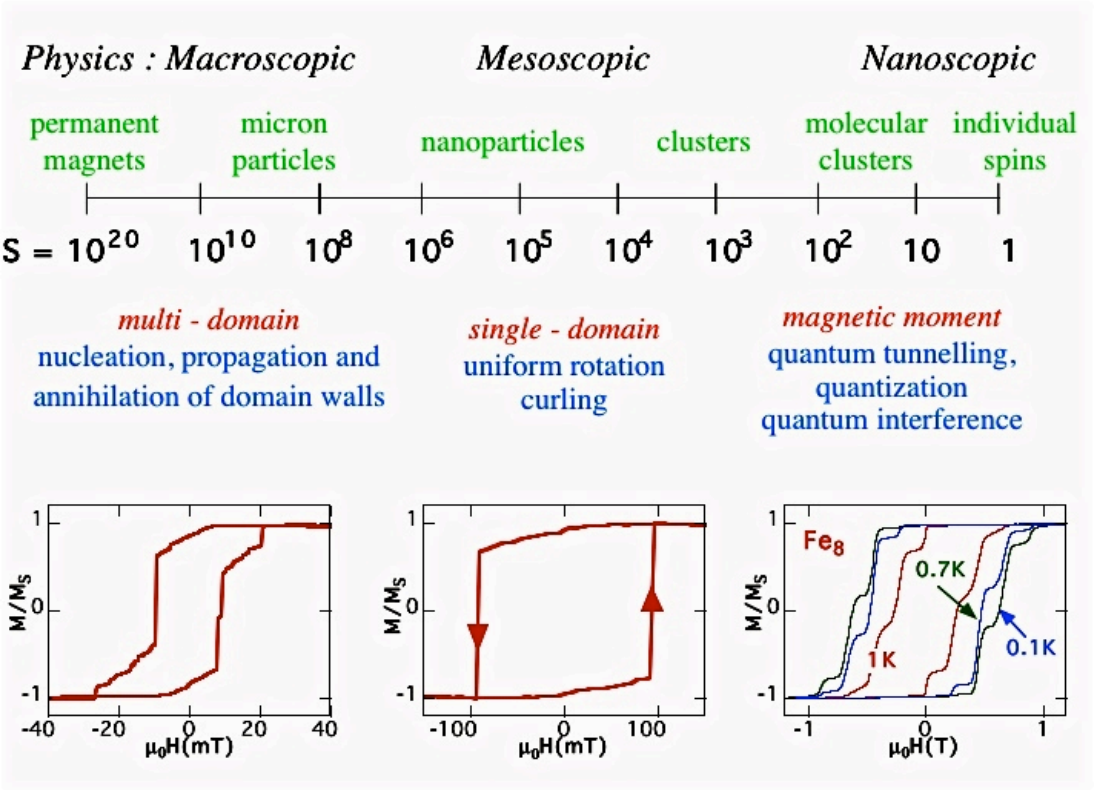

Figure 4. A variety of hysteresis loops showing the magnetization as a function of the application of a magnetic field, and the change in the nature of the loop as the size of the changes in magnetic moment.[5]

Nanostructures with a grain size in the range of <100 nm usually exhibit a single magnetic domain. This property is important because the magnetization of these materials results not from the domain wall movements but, instead, through the coherent rotation of the magnetic moments within the material. As this mechanism costs more energy, destabilizing the magnetic domain after it has been formed is more difficult. Having single domain particles hence raises the values of both the remanent magnetization and the coercivity, and produces magnetic materials that are harder than the soft materials that have low remanence and coercivity values.[6] However, when

the particle size is reduced below the single domain size, a critical diameter is reached, and superparamagnetic behaviour occurs, which results in zero values for coercivity and remanent magnetization, as shown theoretically by Néel.[7] Stable magnetization can not be obtained in superparamagnetic particles due to the thermal fluctuations that cause a frequent reversal of the magnetization in a zero magnetic field. In an applied magnetic field, however, there will be a net magnetic alignment of spin moments with strong reliance on temperature. The nature of the magnetic hysteresis loop is a relatively accurate reflection of the nature of the domain states in the particle (Figure 4). For multi-domain particles, the loops are typically thinner than those for single-domain particles, which usually have a square-shaped loop, due to the large remanence and coercivity values. Particles that exhibit superparamagnetic behaviour have a relatively thin hysteresis loop, which is an indication that both the remanence and coercivity values tend to zero.[8] An illustration of a case in which the coercivity value changes as the particle size changes is shown in Figure 5.

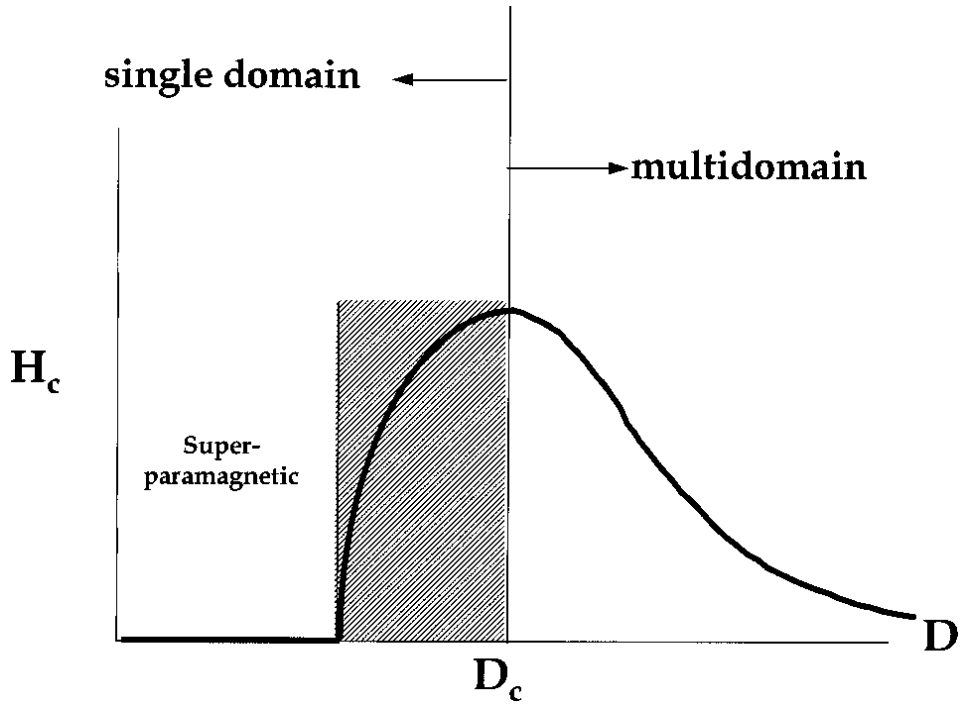

Figure 5. An illustration of how changes in particle size affect the behavior of coercivity.[9]

1.3 Magnetic Data Storage

Since the first data storage device was introduced by IBM in the late 1950s, scientists and engineers have devoted a great deal of attention to developing and increasing the capacity and efficiency of these important devices. As illustrated previously, fabrication of these magnetic devices requires specific materials that exhibit magnetic properties and critical particle sizes. For this process, the main goal is to create devices with high areal density. Nanoparticles with magnetic properties are thus considered very important because their size is generally in the range of single magnetic domains. Obtaining magnetic nanoparticles is therefore very valuable.[10]

Magnetic nanoparticles are very reactive and have a highly spontaneous tendency toward aggregation. Moreover, most magnetic materials that have the potential for use in advanced

technologies are used mainly as films or packed materials, which causes deterioration in their unique magnetic properties. If the magnetic properties of nanomagnetic materials can be retained after compaction, these materials can be excellent precursors for the preparation of a variety of permanent magnets. A highly promising way of stabilizing these materials and of preventing spontaneous aggregation, or oxidation, is to introduce the magnetic nanoparticles into a proper matrix. Such encapsulation of magnetic nanoparticles in a matrix creates very good candidates for data recording devices. Synthesizing magnetic nanoparticles within mesoporous silica thus should helps to stablize them and render them easily processable into objects of any desired shape.

The synthesis of nanoparticles is not the only goal in the preparation of magnetic devices for data storage: these particles must be embedded in a matrix that will also keep them homogeneously distributed and will ensure that the device can be easily manipulated. A first method of meeting these additional goals is based on the initial synthesis of the nanoparticles, followed by their further insertion into a matrix shaped according to the data storage requirements. However, this method can present difficulties, especially with respect to achieving a homogeneous distribution of nanoparticles within the matrix. Another method, which was chosen for the research presented in this thesis, is based on the synthesis of the magnetic centres in parallel with the matrix itself, with the matrix being flexible enough to allow the final shaping as a thick or thin film.

Based on these considerations, for this research, the decision was to synthesize nanocomposite materials that contain magnetic nanoparticles embedded in a diamagnetic matrix. The

nanoparticles were made of molecular-based magnetic materials, such as Prussian blue analogues (PBAs), that provide a high degree of versatility with respect to composition and properties. The matrix was made of mesostructured silica prepared according to a process that allowed one-pot synthesis of nanoparticles inside the silica framework.[11] As well, the formation mechanism of the silica matrix was such that the particle growth is confined within a given region, which permits control of the size of the particles and ensures excellent homogeneity.

1.4 Magnetic Materials

Molecular-based magnets, especially Prussian blue analogues (PBAs), are very versatile materials that can be easily designed through suitable combinations of metal ions and organic linkers. The extreme variety of elements makes these compounds the perfect "guinea pigs" for studying how molecular structure can modify magnetic properties.[12] The expectation was that their use could lead to a new generation of magnets with adaptive properties,[13-14] but no such application has been claimed or demonstrated until now, and current research activity is directed mainly toward their potential for H_2 and other gas storage, especially if porosity can be combined with magnetism.[15-16] At the same time, significant promise has been indicated with respect to the ability to tune their properties, especially magnetism, by tuning the particle size down to the nanoscale.[17- 18] Many syntheses of metallic, bimetallic, or metal oxide magnetic nanomaterials, such as Sm-based intermetallic compounds,[19] cobalt,[20] or iron oxides, respectively, have therefore been reported. Because the achievement of nanomagnet-based systems, especially for data storage, requires that nanoparticles be homogeneously embedded in a diamagnetic matrix, and based on the article about the synthesis of PBA nanoparticles in mesostructured silica,[21-22] it

was determined that this research would explore whether the tailor-made synthesis of molecular-based materials could be the first step in the preparation of metal and metal oxide nanoparticles embedded in a silica matrix.

1.4.1 Metal oxides and metal alloys

The PBA nanocomposites mentioned above were used for this work, as precursors for the preparation of metal and metal-oxide-silica nanocomposites. the adapted thermal treatment was applied to the initial PBA-silica materials for the direct acquisition of metal and mixed-metal oxide nanoparticles embedded in the silica matrix. The goal was to obtain bimetallic oxides, which offer a wide range of magnetic properties. In fact, a number of mixed-metal oxides, such as spinels and perovskites, are well known for their magnetic properties.

Spinel metal oxides have the formula AB_2O_4, where A is a divalent metal ion such as Fe, Ni, or Cu, and B is a trivalent metal ion. The magnetic properties exhibited by these oxides are vital for industrial applications. Ferrite and magnetite are common examples of spinel structures. For example, AFe_2O_4 is the ferrite formula in which A is a divalent metal ion (Fe, Ni, Cu, etc...), and B is $Fe^{(III)}$. Perovskites are another important class of metal oxides with the formula ABO_3, where A and B are cations and the sum of their charges is (+6). This tunable oxidative aspect of this type oxide is very interesting, and it has also been reported that some perovskite composites have ferromagnetic properties.[23] To improve on the usual synthesis methods, our challenge was to obtain the correct degree of oxidation, either by adjusting the initial precursors or by adapting the method of treatment after synthesis.

$SmCo_5$ is a lanthanide-based intermetallic compound that has relatively high values for coercivity and Curie temperature.[24] A coercivity value of up to 10 kOe at a temperature of 500˚C

has been reported for SmCo alloys,[25] making them potentially very valuable for many applications, such as data storage.[26]

1.4.2 Prussian blue analogues (PBA)

The first molecule-based magnetic materials were discovered accidentally by Diesbach in Berlin in 1704. These solids, which are the basis for the Prussian blue analogues (PBAs), attracted a great deal of initial attention because of their colour (Figure 6), and they were used as pigments.

Figure 6. The specific blue colour of Prussian blue $Fe^{III}_4[Fe^{II}(CN)_6]_3 \cdot zH_2O$.

It later appeared that these solids exhibit interesting magnetic properties that can be tuned through changes to their composition and structure, which explains why for many years, they have been considered possible good candidates for technological and industrial applications.[27] These compounds can be synthesized by a simple Lewis acid-base interaction.

$$x[M(H_2O)_6]^{y+} + y[M'(CN)_6]^{x-} \rightarrow M_x[M'(CN)_6]_y \cdot zH_2O \qquad (2)$$

where M and M′ are metal atoms. Most Prussian blue analogues have a simple face-centred cubic lattice (Figure 7).

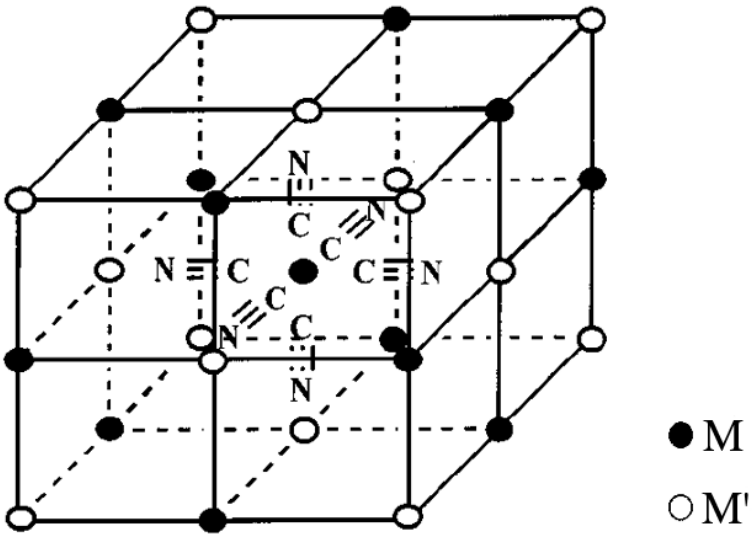

Figure 7. Cubic structure of Prussian blue analogues.[28]

These hexacyanometalate-based compounds display a long-range magnetic order due to the coupling exchange between two transitional metal centres through the cyano bridging ligands CN. Moreover, and because of their unique electronic configuration, the magnetic properties of Prussian blue analogues (PBAs) can be tuned and tailored simply through changes to the transition metal oxidation state, or stoichiometry.[29] The first synthesis reported for the preparation of nanoparticles (NP) of Prussian blue analogues was based on using reverse microemulsions as nanoreactors.[30] These first successful syntheses of well-dispersed, small particles were followed by several studies that employed different ways of synthesizing PBA NPs, including the use of polymers,[31] reduction processes,[32] reverse micelles,[33] porous alumina,[34]

and porous silica.[35] Nanocasting [36] is also a general means of synthesizing PBA nanoparticles, which entails the use of a solid porous matrix that controls the growth of particles and provides a spatial confinement by means of the shape and size of the porous matrix. This method, however, has disadvantages, the most common of which is limited growth of the particles outside the pores of the matrix.

1.5 Silica As a Matrix: Integrative Synthesis and the Sol-Gel Method

Different approaches to the synthesis of organized inorganic nanostructured materials, which include the use of soft templates and the use of cooperative assemblies of building blocks combined with soft templates, were first described by Stephen Mann,[37] and Clement Sanchez.[38] They refereed to "*integrative syntheses*". Their work has recently been updated by Backov,[39] who defined this kind of process as one in which the combination of different soft chemistry processes with soft matter is achieved based on the concept of "*Integrative Chemistry*". Sol-gel methods are a major component of Integrative Chemistry. They are a room-temperature solution approach that allows the preparation of homogeneous solid materials from molecular precursors, by using either an aqueous, or a non-aqueous solvent. The more general term of “Chimie Douce,” or soft chemistry, was proposed in the 1980s by Jacques Livage and Jean Rouxel to include all room or medium temperature methods that allow for the synthesis of inorganic solid phases, usually prepared at higher temperatures. Such a process is in contrast with the traditional "*shake & bake*" solid chemistry method in which the final material is obtained through the solid

state diffusion and reaction of elements, a high temperature, so that a stable thermodynamic state is finally achieved.

Sol-gel methods are versatile and can employ different organometallic precursors, solvents, temperatures, and catalyst concentrations in order to generate an end product with a variety of shapes and sizes that can be tailored to meet the requirements of the final application. Hydrolysis and condensation of the organometallic precursor are the two main reactions in the sol-gel process that lead to the formation of an amorphous silica glass after solvent natural (xerogel) or supercritical (aerogel) evaporation.

Hydrolysis occurs when the organometallic precursors, most commonly tetraethoxysilane, are made more reactive through dissolution in water or alcohol in order to generate the Si-OH species. Condensation takes place when those reactive precursors react together to generate the solid network Si-O-Si. Two reactions occur at this stage with a fast one (olation) leading to Si-OH-Si connections, and a slower one (oxolation) giving Si-O-Si bonds. This latter creates shorter bonds, which results at the macroscopic scale, into a continuous shrinking of the gel, even under wet conditions, called syneresis. When the condensation is almost fully achieved, a gel that consists of a continuous Si –O–Si (oxo groups) bonded network is expected, but some SiOH species that have not completely reacted, or Si-OH-Si (ol groups) remain. Upon drying, the gel shrinks due to the solvent evaporation, and a major fragmentation can be observed if the drying process does not take into account internal capillary forces. The final xerogel that forms is strong, highly porous, and transparent. This mechanism of silicate formation from alkoxides

through hydrolysis and condensation has been described by Brinker [40] as occurring in three steps (Figure 8).

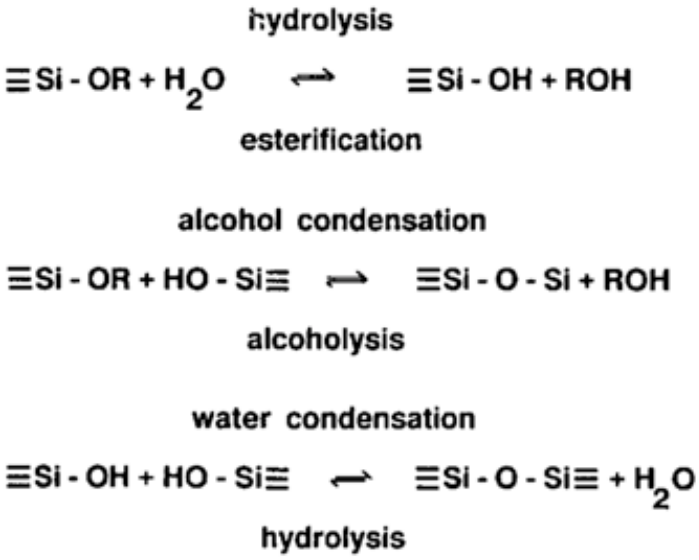

Figure 8. Three-step hydrolysis and condensation mechanism for silicon alkoxide.[40]

1.5.1 Synthesis of mesoporous materials

Mesoporous silica has been regarded as an intriguing material due to its high porosity and large surface area, and to the fact that its pore size can be tuned and modified based on different parameters. In 1990, the first templated mesoporous silica was discovered by a group of researchers in Japan.[41] However, the first family of highly ordered mesoporous M41S was reported by Mobil company researchers in 1992, the first group to refer to a liquid-crystal template mechanism. They used a cationic surfactant of alkyl ammonium as the structure-directing agent during the sol-gel synthesis.[42] Since, different types of mesoporous silica have been formed, depending on the initial materials and variations in the synthesis conditions. In

1998, the SBA-silica type was reported by a group of researchers from the University of California in Santa Barbara.[43] To date, a number of mesoporous materials have been synthesized using cationic surfactants as templating agents, such as KIT-n,[44] HMS-n,[45] and FDU-n.[46] The synthesis of mesoporous silica with the use of nonionic poly (ethylene oxide) surfactants has also been described, and is called MSU.[47-48]All of these syntheses use the silica sol-gel process as the method of building the inorganic framework.

During the synthesis of mesoporous materials, organic molecules such as a surfactant can serve as a mold or a template, around which a solid framework can be built. The removal of this template results in a porous network that retains a structure and morphology almost identical to those of the self-assembled molecules. This process is called the soft-template approach (Figure 9).

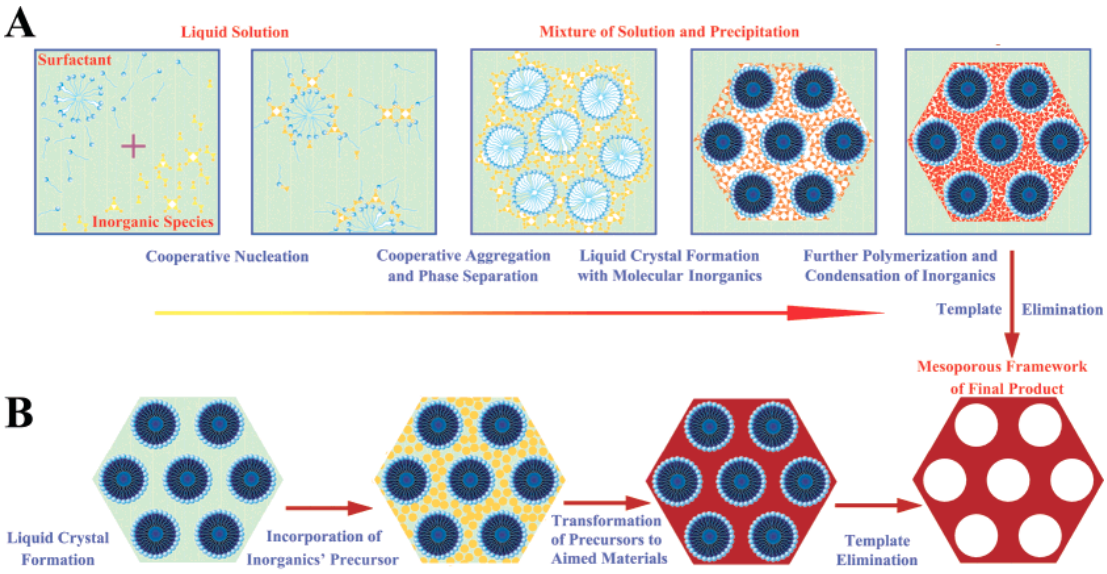

Figure 9. Different synthetic approaches for mesoporous: (A) cooperative surfactant self-assembly; (B) templating process using a "true" liquid-crystal.[49]

Studies have been carried out to investigate the formation of silica mesostructures based on the surfactant self-assembly template and sol-gel methods. During the synthesis of inorganic-organic mesostructured composites, the sol-gel process is involved in the interaction between the self-assembled surfactant and the silicate. It is recognized that the sol-gel route is appropriate and very advantageous with respect to the synthesis of mesoporous silica: when synthesis parameters such as the temperature and the pH value are modified, the rates of both the hydrolysis and the condensation of the silicates can be easily controlled.

MSU silica is recognized as the first material that was prepared with the use of a nonionic surfactant, polyethylene oxide (PEO), for the synthesis of micromesoporous silica. PEOs are nontoxic, inexpensive, and biodegradable. For this neutral templating route, hydrogen bonds are considered to be the major driving force in the formation of the mesophase.

A two-step synthesis was developed for the MSU-X silica: first, the self-assembly that occurs because of the interaction between surfactants and silica oligomers results in the formation of stable hybrid micelles, followed by catalysis-induced silica condensation. In this synthesis, reaction parameters such as temperature and pH cause significant changes in the final pore size. This two-step synthesis can be further modified because of the advantage provided by the stability of the self-assembled inorganic/organic hybrid micellar structures, known as the hybrid micelle concentration (HMC) process (Figure 10). This process can then be concentrated through the controlled evaporation of water to produce monolithic gels rather than particles, without the help of a catalyst.[11] Such a reaction allows for the addition of other components (ions, molecules,

particles) that are entrapped within the mesoporous matrix once the silica condensation has occurred.

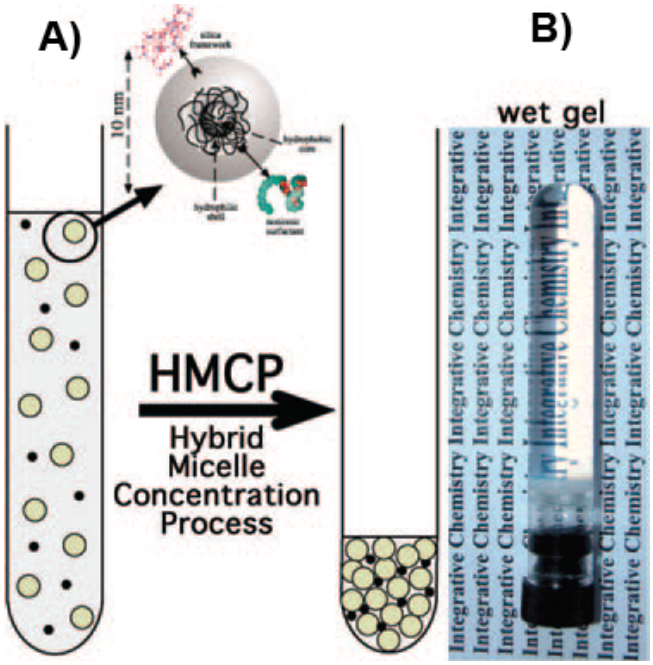

Figure 10. (A) A hybrid micelles concentration solution is mixed with other components (• = ions, molecules, particles). (B) The concentration process is induced by evaporation to obtain a transparent homogeneous gel which traps the different elements so that they are homogeneously stabilized and dispersed within the gel.[11]

In this work, mesoporous MSU silica was used as the host matrix that embeds and stabilizes PBAs. PBA precursors are initially added to the concentrated solution of hybrid micelles, and they react rapidly in parallel with the gelation of the mesostructured silica gel. The high viscosity and confinement provided by the silica gelling mechanism prevents the PBA particles from aggregating and growing, and a final nanocomposite material with PBA nanoparticles homogeneously distributed within the silica gel, results from this one-pot reaction.

Chapter 2

Research Project, Synthetic Methods, and Analysis Tools

2.1 Research Project

From a fundamental perspective, molecular-based magnetic materials such as PBA nanoparticles exhibit interesting magnetic properties. However, in spite of their great promise, they do not seem to be suitable for actual applications, due either to their low Curie temperature (a few Kelvins) when they are stable in air or to their instability in air when they are magnetic at room temperature. These nanocomposites are nevertheless potentially good candidates for the preparation of bimetallic nanoparticles and oxides through controlled thermal treatment. Therefore, the research conducted for this thesis was focused on these two nanoparticle classes, with the goal being the synthesis of permanent nanomagnets made from bimetallic alloys, such as SmCo or SmFe alloys, which appear to be the best candidates for data storage.

The development of devices that use a magnetic centre also requires the ability to prepare materials that have a high-density magnetic centre. Previous studies[22] in this project, have not addressed this question and describe only materials that have low concentrations of PBAs. Hence, the research presented in this thesis represents a major step forward in this development.

The original synthesis was initially reported for silica-embedded hexacyano polymetallate $Co^{(II)}_3[Fe^{(III)}(CN)_6]_2$; other compounds have been synthesized using $Ni^{(II)}_3[Co^{(III)}(CN)_6]_2$, $Fe^{(II)}_3[Co^{(III)}(CN)_6]_2$, $Co^{(II)}_3[Co^{(III)}(CN)_6]_2$, $Co^{(II)}_3[Fe^{(III)}(CN)_6]_2$, and $Ni^{(II)}_3[Fe^{(III)}(CN)_6]_2$ with a low concentration (0.8 mol%) inside a silica mesostructured matrix.[22] Based on these

considerations, this research work focused on synthesizing $Ni^{(II)}_3[Co^{(III)}(CN)_6]_2$, $Co^{(II)}_3[Co^{(III)}(CN)_6]_2$, and $Sm^{(III)}[Co^{(III)}(CN)_6]$, with different objectives than those previously reported. The primary goals were (i) to determine whether or not similar materials could be synthesized with different composition, (ii) at higher concentrations and (iii) what would be their chemical and structural evolution as a function of concentration after thermal treatment, depending on the thermal treatment parameters.

The nanoparticles were made of molecular-based magnetic materials, such as PBAs, that provide a high degree of versatility with respect to composition and properties. The matrix was made of mesostructured silica prepared according to a process that allowed one-pot synthesis of the nanoparticles inside the silica framework. As well, the formation mechanism of the silica matrix was such that the particle growth was confined within a given region, permitting control of the size of the particles and ensures excellent homogeneity.

The calcination of the obtained PBA nanocomposite allowed the removal of the surfactant and cyano-group from the nanocomposite, permitting the bimetallic nanoparticles that are not cyano-bridged to be obtained in the silica matrix.

2.2 Experimental methods

The synthesis used in this research was based on a work previously carried out and reported in Pr. Prouzet' group,[22] but the nature of phases and the range of PBA concentrations differed completely from the previous study. In a typical synthesis, 5.7 g of a nonionic polyethyleneoxide (PEO)-based surfactant (Brij 98) are first dissolved in 50 mL of deionized water (pH 2). After

full dissolution, 20.5 g of tetraethylorthosilicate (TEOS) ($Si(OCH_2CH_3)_4$) is added drop by drop to the mixture under magnetic stirring. The solution, initially cloudy, turns to transparent as TEOS is progressively hydrolyzed. Once the mixture is fully transparent, the solution is covered by Parafilm and left to age in a refrigerator overnight. An amount of 4.2×10^{-3} mol of metal salt diluted in 5 mL of DI water is then added, and the mixture is concentrated in a Rotavapor through evaporation at 40 ˚C in a dynamic vacuum, until 50 wt% of the total mass is removed. The synthesis of the PBA is then initiated by the addition of 2.8×10^{-3} mol of potassium cobaltohexacyanate $K_3Co(CN)_6$ diluted in 5 mL of DI water at pH = 2. The formation of PBA is immediate, and the evaporation is then continued to completion. The solid phase is recovered and dried in the oven at 65 C˚ overnight. The general procedure scheme for the synthesis of PBA@MSU is shown in Figure 11, and all of the specific concentrations used in this research are shown in Table 1 for the NiCo PBAs@MSU, Table 2 for the CoCo PBAs@MSU, and Table 3 for the for the Sm Co PBAs@MSU.

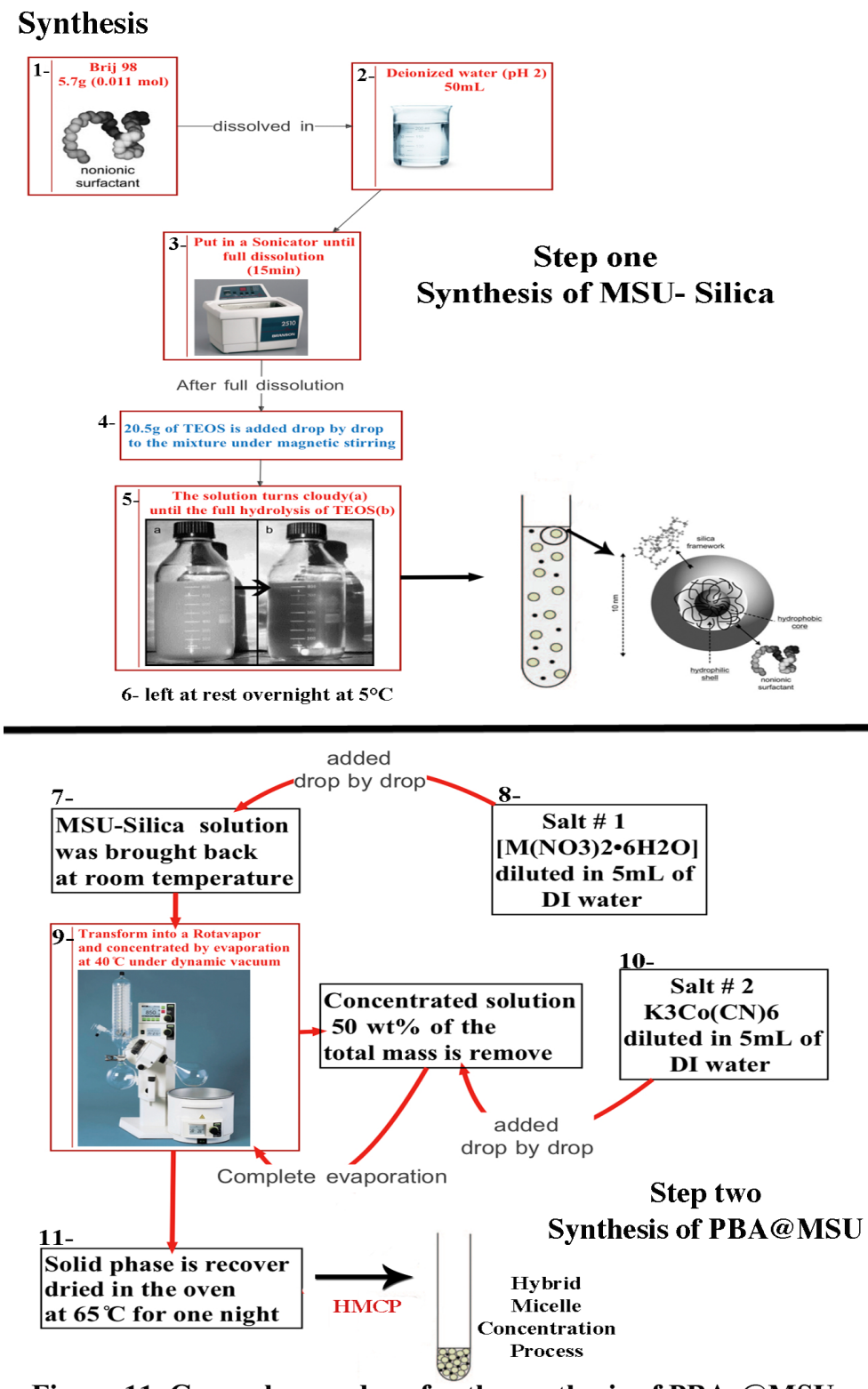

Figure 11. General procedure for the synthesis of PBAs@MSU

2.3 Characterization Techniques

2.3.1 Small Angle X-ray Scattering (SAXS)

The small-angle X-ray scattering (SAXS) is used to obtain information not only about crystalline materials but also about amorphous materials, as far as some correlated electron density contrast exists. The size of small particles can be also determined by analyzing the intensity of the X-ray in the small 2θ range from about 2θ = 0.1° to 5°. Amorphous materials do not have a long-range order, however, their pore structure can exhibit a long-range order or distance correlations that can be probed by SAXS. Therefore, at small 2θ ranges, the peaks observed can provide useful information about the pore structure and size. SAXS is a technique that permits an examination of the difference (contrast) between regions with different electron densities: one example is pores in aggregates, or packing of particles. With this method, scattering patterns are reported as a function of the scattering wave vector q (nm^{-1}) rather than the 2θ (degree), where q is the difference between the wave vectors of the incident and the scattered waves. The value of q can hence be defined based on Bragg's law, as follows:

$$d = 2\pi / q \tag{3}$$

where d is the correlation length (also called "d-spacing" if no specific crystal indexation exists). Thus, θ and q are related by the following:

$$q = 4\pi \sin\theta / \lambda \tag{4}$$

SAXS measurements were carried out on a SAXSess system (Anton Paar) that uses SAXSquant and OptiQuant programs, operating with a 2.2 kW copper anode (λ=1.54Å) from 2θ = 0° to 40°.

2.3.2 X-ray Powder diffraction (XRD)

X-ray powder diffraction (XRD) is a powerful technique that allows the determination of crystal structures, the identification of different crystalline materials, and the recognition of different phases in a mixture according to the diffraction peaks obtained. This technique is also used for the determination of crystallite size based on an analysis of the peak broadening. Using Bragg's law, interplanar distances d can also be obtained based on the relationship between the X-ray wavelength λ and the angle of incidence of the X-ray beam 2θ:

$$\lambda = 2d\sin\theta \tag{5}$$

The XRD patterns of all samples were obtained with the use of a Bruker D8-ADVANCE powder diffractometer operating at 40 kV and using Cu Kα radiation (λ = 1.5405 Å) operating from 2θ = 5° to 70°.

TP-XRD was performed with an Inel CPS120 equipped with a FUR1400 high temperature furnace. The sample was left to equilibrate for 10 min at the given temperature before measurement (10 min recording time).

2.3.3 Fourier transform infrared spectroscopy (FTIR)

Fourier transform infrared spectroscopy (FTIR) is an analytical technique used to obtain information about the molecular structure of a material. The functionality of this technique is based on the principle that most molecules can absorb infrared light. Because each type of

molecule absorbs infrared light at those frequencies where the dipolar moment of the molecule is affected by the infrared light, the resulting spectrum represents a fingerprint pattern for each molecule. For this research, FT-IR spectra were recorded from 400 to 4,000 cm^{-1} (16 scans, 0.2 cm^{-1}) under transmission with a Brucker Tensor 27 spectrometer (OPUS program). The absorption was adjusted by mixing the samples with KBr (Fisher Scientific).

2.3.4 Transmission Electron Microscopy (TEM)

The transmission electron microscopy is a powerful analytical technique that permits detailed structural analysis with high magnification and resolution. It also allows an examination of chemical composition, crystal orientation, and structure. A TEM can provide images of the atomic orientation of a single crystal. Structural investigation of vacancies and defect sites is also possible. The ability to obtain high resolution is one of the major advantages of TEM, but it can be destructive to some samples and is relatively expensive. The preparation of the sample can also be time consuming. For this research , TEM samples were prepared using extractive replicas of ultramicrotomy techniques deposited onto copper grids. TEM measurements were carried out at 100kV with a JEOL 1200 EXII microscope

2.3.5 Scanning Electron Microscopy (SEM)

Scanning electron microscopy (SEM) is an effective method for investigating the surface structure, shape, and size of particles as well as the composition and relative amounts of the elements and compounds in a sample. High-resolution 3D images can be obtained for gold-coated samples using the SEM technique. In this research, a Leo 1530 microscope at an EHT of 5 kV SEM was used.

2.3.6 Magnetic Measurements (SQUID) and (PPMS)

Magnetic susceptibility data were collected with a Quantum Design MPMS-XL SQUID magnetometer working in a temperature range of 1.8–300 K and the magnetic field range of 0–50 kOe. The data were corrected for the sample holder. A SQUID magnetometer is very sensitive to fluctuations in the magnetic field. AC measurements are very useful for describing and validating the properties of superparamagnets and spin-glasses. For this work, AC magnetic measurements were also recorded by means of a physical property measurement system (PPMS), Quantum Design in ACMS mode, using a helium cooling system. The overall magnetization levels were measured as a function of the applied magnetic field.

Chapter 3

Synthesis of PBA Nanoparticles with a Variety of Transition Metals Using Silica matrix

3.1 $Ni_3[Co(CN)_6]_2$ Synthesis and Analysis

A nickel (II) cobalt (III) Prussian blue analogues (PBA) has previously been studied and prepared using low PBA concentrations. The first part of this chapter focuses on the fabrication of NiCo PBAs in an MSU silica nanocomposite material with relatively higher concentration, Table 1 shows the structural parameters of NiCo-PBA@MSU with six different concentrations ranging from 12.5 wt% to 35wt % of the PBAs in the silica. The precipitation of the NiCo-PBA is controlled at nanoscale dimensions by the silica network gelation. The resulting nanocomposites are homogeneous and exhibit no evidence of particle separation out of the silica matrix, as will be further discussed later in this chapter. These materials suggest that a new approach for the utilization of the nanoparticle with a higher concentration in PBA embedded homogeneously in a silica matrix, is allowed, which fits potentially with their application in advanced magnetic devices. Table 1 displays the structural parameters of all concentrations of the NiCo PBAs @MSU silica

Table 1: Structural Parameters of NiCo-PBA@MSU (PBA Synthesised into 5.9 g / 0.098 mol of SiO_2)

NiCo(x wt%)-PBA@MSU	$Ni(NO_3)_2.6H_2O$ (g/*mol*)	$K_3Co(CN)_6$ (g/*mol*)	$[Ni(NO_3)_2.6H_2O]$ / $[K_3Co(CN)_6]$ (g/*mol*) ratio	PBA (g/*mol*)	PBA/(PBA + SiO_2) wt% / *mol %*	d spacing (nm)
NiCo(12.5%)	1.42/*4.2 10^{-3}*	0.95/*2.8 10^{-3}*	1.5/*1.7*	0.84/*1.4 10^{-3}*	12.5/*1.4*	6.2/ 5.2

NiCo(22%)	2.85/*9.8 10^{-3}*	1.90/*5.7 10^{-3}*	1.5 /*1.7*	1.70/*2.3 5 10^{-3}*	22/*2.3*	6.2
NiCo(25%)	3.23/*11.0 10^{-3}*	2.21/*6.6 10^{-3}*	1.5 /*1.7*	2.0/*3.3 10^{-3}*	25/*3.2*	6.2
NiCo(29%)	3.88/*13.3 10^{-3}*	2.65/*7.9 10^{-3}*	1.5/*1.7*	2.4/*3.95 10^{-3}*	29/*3.9*	6.2 nm
NiCo(31%)	4.27/*14.0 10^{-3}*	3.00/*9.0 10^{-3}*	1.4/*1.7*	2.72/*4.5 10^{-3}*	31/*4.4*	6.2 nm
NiCo(35%)	5.12/*17.6 10^{-3}*	3.60/*10.8 10^{-3}*	1.4 /*1.7*	3.27/*5.4 10^{-3}*	35/*5.2*	7.1 nm

3.1.1 Influence of higher NiCo PBA concentrations on the silica matrix

Figure 12 displays the SAXS pattern of NiCo-PBA@MSU prepared with different amounts of PBA, quantified by the (PBA/PBA+SiO_2) wt% ratio. All SAXS patterns exhibit at least one peak at approximately 1 nm^{-1}, as a clear indication of a mesostructured order (the organic templates have not been removed).

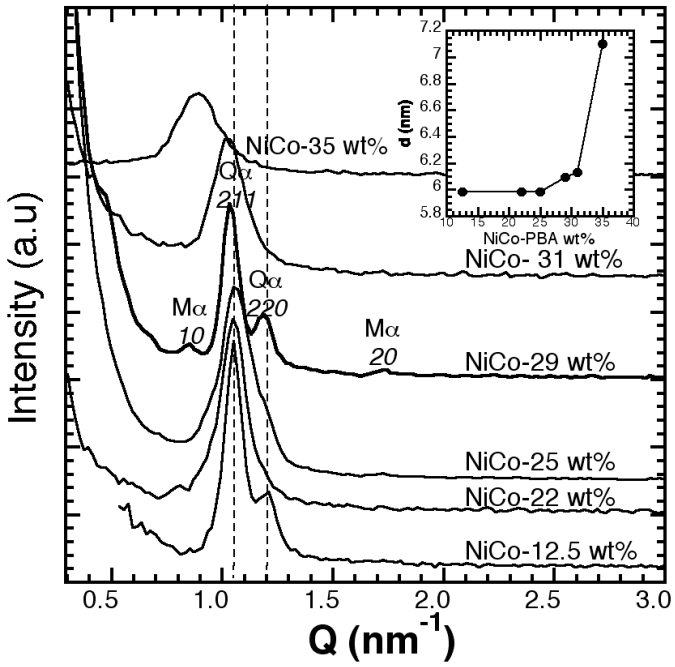

Figure 12. Evolution of the SAXS pattern for NiCo-PBA@MSU prepared with different (PBA/PBA+SiO_2) wt% ratio.

This mesostructure results from increasing the relative concentration of the surfactants, which results in the water evaporation during the evaporator step, allowing the system to shift from the domain of micelles to that of liquid crystals.[50] The NiCo-29wt% sample, with the more clear pattern, illustrates particularly the general mechanism of formation of this mesostructure: two intense peaks at 1.03 and 1.18 nm^{-1}, which can be assigned to a cubic Q_α ({*211*} and {*220*}), and two others at 0.84 and 1.73 nm^{-1} that can be assigned to a minor hexagonal M_α ({*10*} and {*20*}), as reported by Auvray *et al*.[51] This sample contains two concomitant mesophases, but the cubic one is predominant. The same cubic phase is identified for the samples prepared with a lower content of PBA (12.5 to 25 wt%), with diffraction peaks that are more or less defined, but clearly

present. Such a cubic structure was not reported in the previous study,[52] but the SAXS apparatus used for that study was not as resolving as the SAXSess system used for the present one.

The NiCo-25wt% sample can even exhibit a minor hexagonal phase, however, further increasing the PBA content over 29 wt% leads to a more disordered structure, with only one single peak being identified. The inset of Figure 12 displays the evolution of the *{211}* peak of the Q_{α} phase as a function of the PBA content. The correlation distance remains constant and equal to 6.0 nm up to 25 wt%. Above this value, the distance increases slightly up to the highest PBA loading (35 wt%) that exhibits a disordered structured with a larger correlation distance (7.1 nm). The variation of the correlation distance is explained by the parallel disturbance induced by the increasing amount of PBA synthesised within the silica matrix.

3.1.2 Validating NiCo PBA nanoparticle formation inside the matrix

The FT-IR spectroscopy of the NiCo PBAs series, (Figure 13), confirms the occurrence of the reaction via the analysis of the ν(CN) stretching mode that shifts from 2,080 cm^{-1} for the unreacted free CN^- ions,[52] to 2,180 cm^{-1} for the $Ni_3[Co(CN)_6]_2$-MSU samples (Table 2 and Figure 14).

Table 2: Infrared bands for MSU-NiCo-PBA@MSU prepared with different concentrations in PBA

Sample	ν (CN) (cm^{-1})	ν (NO_3) (cm^{-1})	δ(OH) (cm^{-1})
MSU-NiCo-12.5%	2183	1385	1635
MSU-NiCo-22%	2183	1384	1633
MSU-NiCo-25%	2183	1384	1631
MSU-NiCo-29%	2182	1384	1635

MSU-NiCo-31%	2183	1384	1630
MSU-NiCo-35%	2182	1384	1635

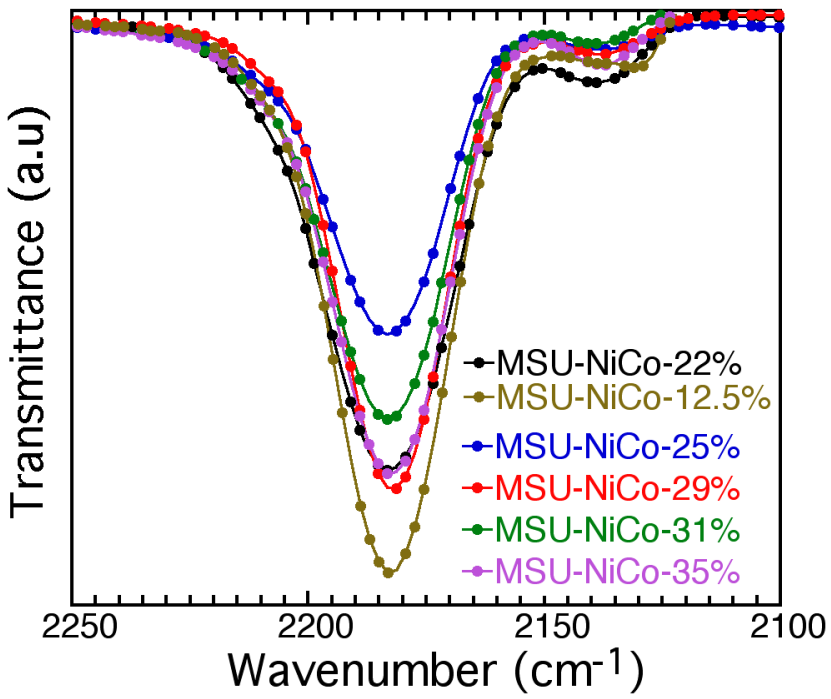

Figure 13. FTIR spectra of NiCo-PBA@MSU synthesised with different concentrations of PBAs (domain of ν(CN)).

A second small peak, appears as a shoulder at 2,137 cm^{-1}.,which was observed for all NiCo samples , including bulk (Figure 15) and low concentration NiCo-PBA@MSU (Figure 16). Its position cannot allow us to assign it to cyanide isomerism, but it could be the result of sites locally disturbed by water molecules, since this contribution, already observed in $Co_3[Co(CN)_6]_2.xH_2O$,[53] disappeared upon further drying.

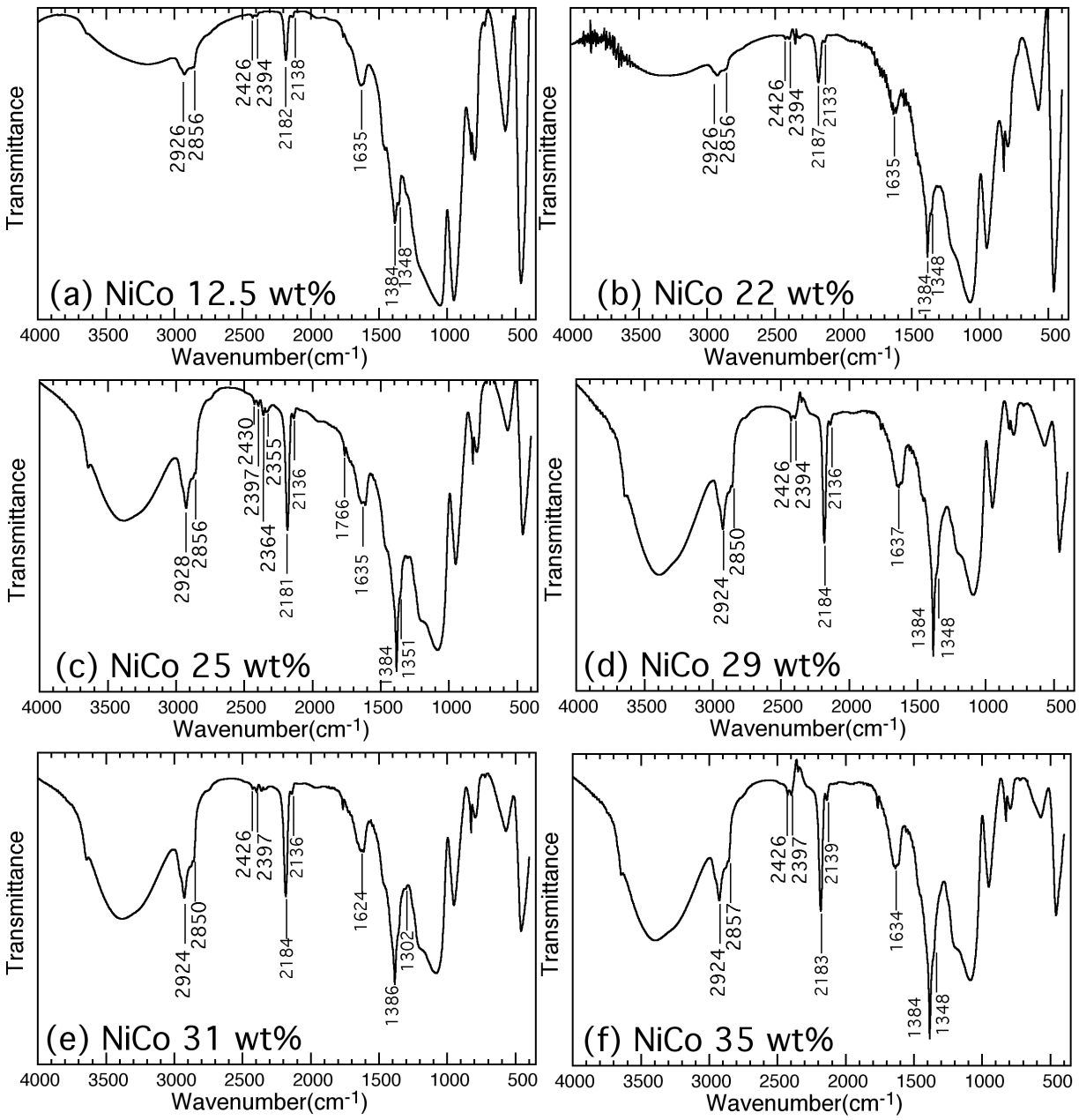

Figure 14. FT-IR spectra of NiCo-PBA@MSU synthesised with higher concentrations in PBA

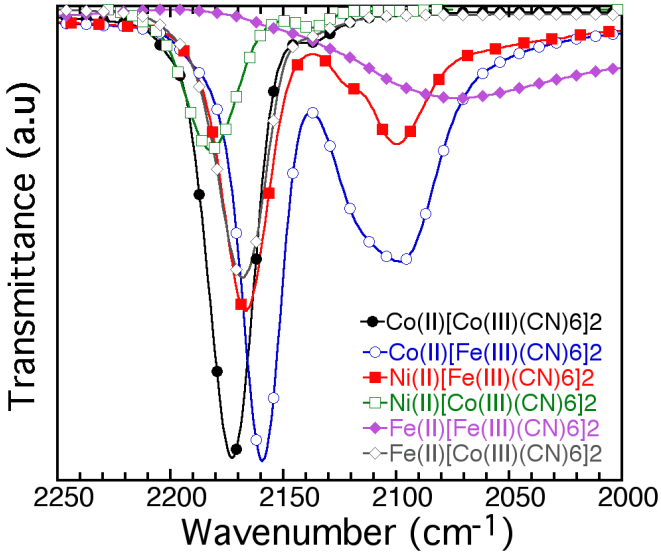

Figure 15. FT-IR spectra of bulk Prussian Blue Analogues

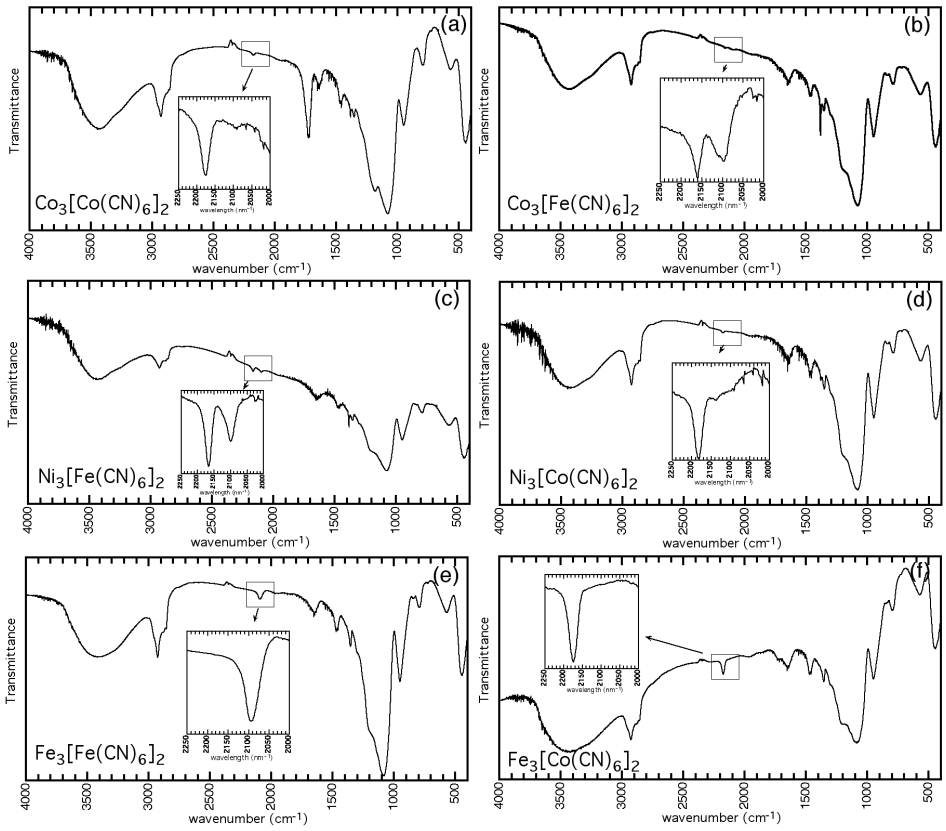

Figure 16. FT-IR spectra of MM'-PBA@MSU synthesized with low concentration in PBA

Figure 17 compares the powder XRD patterns recorded in parallel with the SAXS (recording range limited to 40 degrees) for the different $Ni_3[Co(CN)_6]_2$@MSU samples. All diffraction peaks can be assigned to the *fcc* structure expected for the nickel cobalt hexacyanide.[52, 54] All diffraction patterns are similar and their intensities tend to increase with PBA content.

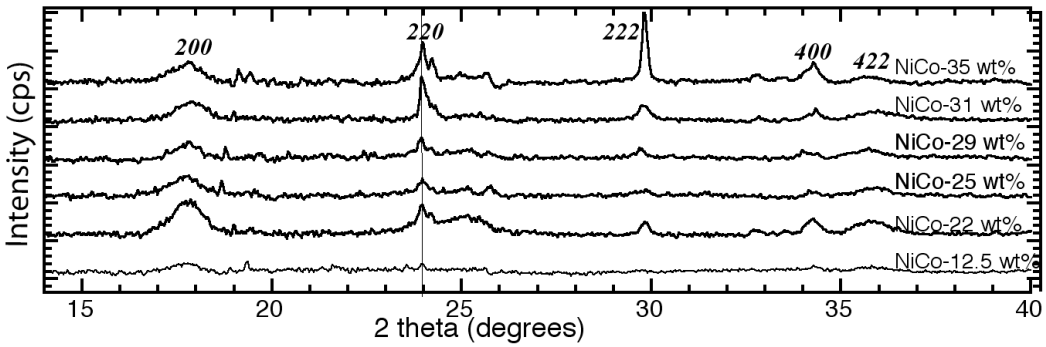

Figure 17. Diffraction pattern of the for the different Ni3[Co(CN)6]2@MSU samples

These different analyses confirmed that PBAs can be synthesised within the mesostructured silica matrix at higher quantities than previously reported. As expected, higher concentrations lead to larger crystals, 10 nm for the 29 wt% $Ni_3[Co(CN)_6]_2$ rather than 4 nm for $Fe_3[Co(CN)_6]_2$, as observed with a low concentration.[52]

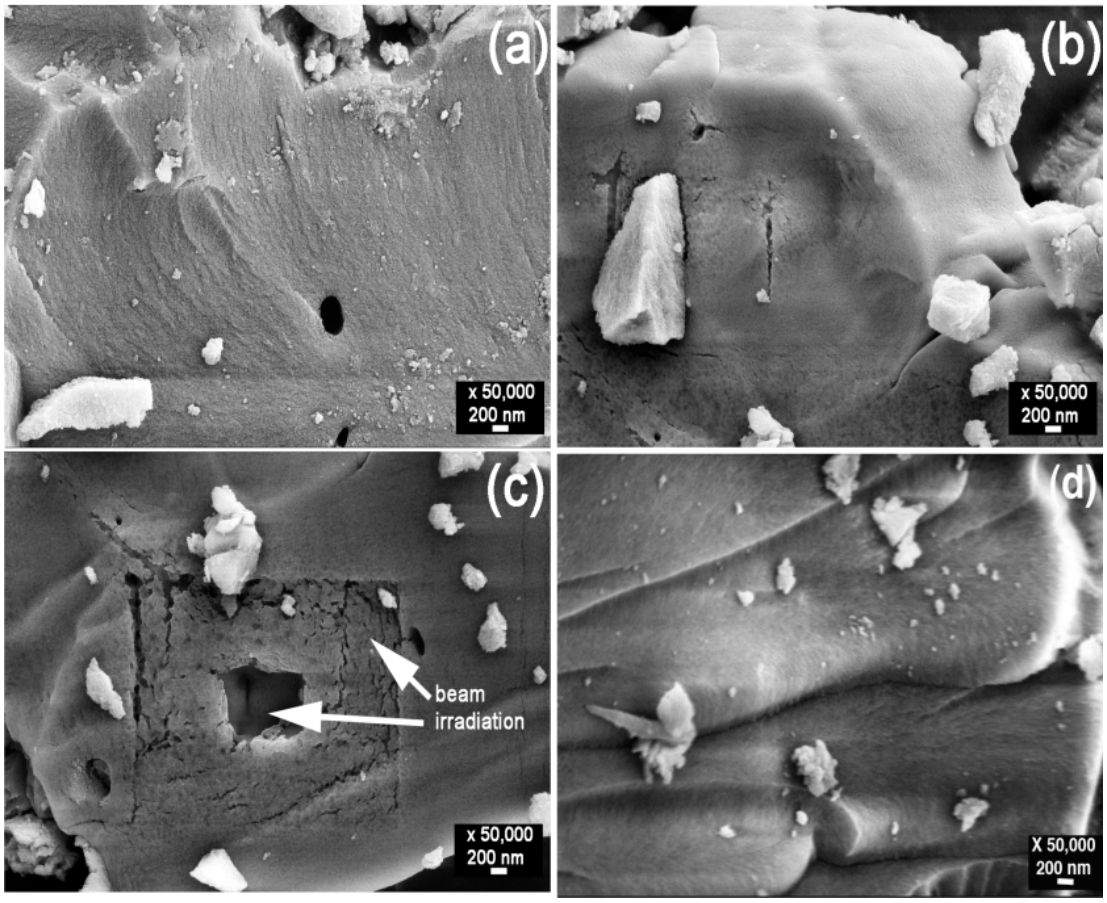

Figure 18. SEM observations of (a) NiCo(12 wt%)- PBA@MSU, (b) and (c) NiCo(35 wt%)-PBA@MSU, and (d) NiCo(29 wt%)-PBA@MSU.

SEM analysis confirms the integration of PBA nanoparticles inside the silica structure and the level of homogeneity (Figure 18). Previous studies conducted in Professor Prouzet's laboratory have demonstrated that, even at low concentrations, different synthesis processes lead to the formation of heterogeneous materials with the crystallisation of PBA crystals outside of the silica host.[52] The present study confirms that these materials can be prepared with the same method, yet at significantly higher concentrations (12 wt%- 25 wt% t rather than 0.8 wt %) and still preserve the homogeneity of the entire structure. As a result, we do not observe any PBA

crystals outside the silica matrix. The increasing concentration leads to a progressive amorphisation of the silica matrix, which becomes significant only for large amounts of PBA (35 wt%). The influence of increasing the amount of PBA beyond a given limit is effectively illustrated by the behaviour of the sample under the electron beam. The samples with 12 wt % and 29 wt % PBA content (Figures 18(a) and 18(d), respectively) show perfect resistance to beam irradiation, whereas the sample with a larger amount of PBA (Figures 18(b) and 18(c) is destroyed within seconds, even with a low energy electron beam (5 kV). The validation of this synthesis at concentrations suitable for future applications in magnetic storage enabled the testing of these materials for use in the preparation of silica-embedded metal and metal oxide magnetic nanoparticles.

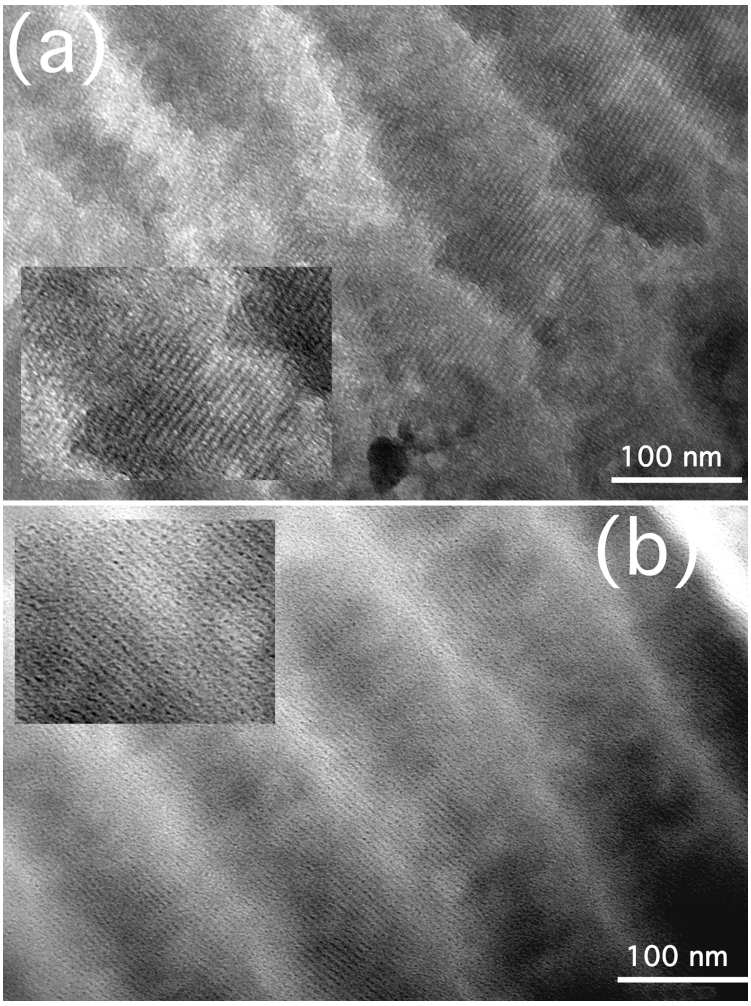

Figure 19. TEM observations of NiCo/29 wt%@ MSU.

The TEM observations of the extractive replica of the NiCo /29/@MSU sample illustrates how the order of the silica mesostructure (Figure 19(a)) directs the alignment of the internal PBA nanoparticles (Figure 19(b)). The two photos, obtained with different adjustments for contrast, clearly demonstrate that the PBA nanoparticles are well aligned along the 2D structure of the mesostructured silica. These photos also show domains that are distributed homogeneously throughout the amorphous silica matrix.

3.2 $Co_3[Co(CN)_6]_2$ Synthesis and Analysis

$Co_3[Co(CN)_6]_2$ nanoparticles have been synthesised using different sizes and morphologies using different approaches.[55-56] In this thesis work, CoCo-PBAs nano-particles were synthesised using MSU-silica as a matrix and with relatively higher concentrations of the CoCo PBAs than in previous work. CoCo PBA ratios ranging from 9.6 wt% to 35 wt% were used (the ratio is (PBA/PBA+SiO_2) wt%). All of the structural parameters for the CoCo PBA samples are displayed in Table 3. SAXS, XRD, and FTIR analyses were carried out for each sample in order to investigate the effect of different concentrations on the silica matrix and on the final PBA product.

Table 3: Structural Parameters of CoCo-PBA@MSU (PBA Synthesised into 5.9 g/0.098 mol of SiO_2)

Sample	$Co(NO_3)_2.6H_2O$ (g/*mol*)	$K_3Co(CN)_6$ *(g/mol)*	$[Co(NO_3)_2.6H_2O]$ / $[K_3Co(CN)_6]$ *(g/mol)*	PBA *(g/mol)*	PBA/(PBA + SiO_2) *wt% / mol %*	d-spacing *nm*
MSU-CoCo-9.6%	0.95 / *3.2 10^{-3}*	0.695/*2.09 10^{-3}*	1.37 / *1.6*	0.63/*1.04 10^{-3}*	9.6/*1.1*	5.7
MSU-CoCo-17%	1.9 / *6.5 10^{-3}*	1.39 / *4.2 10^{-3}*	1.37 / *1.6*	1.27 / *2.1 10^{-3}*	17 / *2.1*	6
MSU-CoCo-21.3%	2.58 / *8.8 10^{-3}*	1.76/*5.3 10^{-3}*	1.46 / *1.6*	1.6/ *2.6 10^{-3}*	21.3/*2.6*	6.9
MSU-CoCo-29%	3.88 / *13.3 10^{-3}*	2.65 / *8.0 10^{-3}*	1.46 / *1.6*	2.42 / *4.0 10^{-3}*	29 / *3.9*	6.2
MSU-CoCo-31%	4.27 / *14.6 10^{-3}*	3 / *9.0 10^{-3}*	1.42 / *1.6*	2.7 / *4.5 10^{-3}*	31 / *4.3*	7
MSU-CoCo-35%	5.12 / *17.5 10^{-3}*	3.6 / *10.8 10^{-3}*	1.42 / *1.6*	3.28 / *5.4 10^{-3}*	35.7 / *5.2*	6.2

3.2.1 Influence of higher CoCo PBA concentrations on the silica matrix

SAXS measurements were carried out for all of the CoCo PBA samples in order to confirm that the mesostructured silica were preserved during the synthesis of the CoCo PBA nanoparticles.

Figure 20 shows the SAXS patterns for the series of CoCo-PBA@MSU samples prepared with CoCo-PBA ($9.6 < x$ wt% < 35.7). All of the SAXS patterns exhibit a correlation peak close to 1.0 nm^{-1}; however, a more ill-ordered structure can be observed for most of the samples. The CoCo-29 wt% can even exhibit a minor hexagonal phase, while samples with 31 % CoCo-PBA@MSU show a specific complex structure, in which the diffraction peaks labeled (*200*), (*210*), and (*211*) indicate a bicontinuous cubic phase formation as reported by Zhou et al.[57] As previously proven for the NiCo-PBAs samples, the aggregation behaviour of the surfactant is controlled by the evaporation rate, and the final structure of the silica is hence governed by the behaviour of the surfactant during the evaporation step, which allows the unexpected cubic and hexagonal mesophase to form.

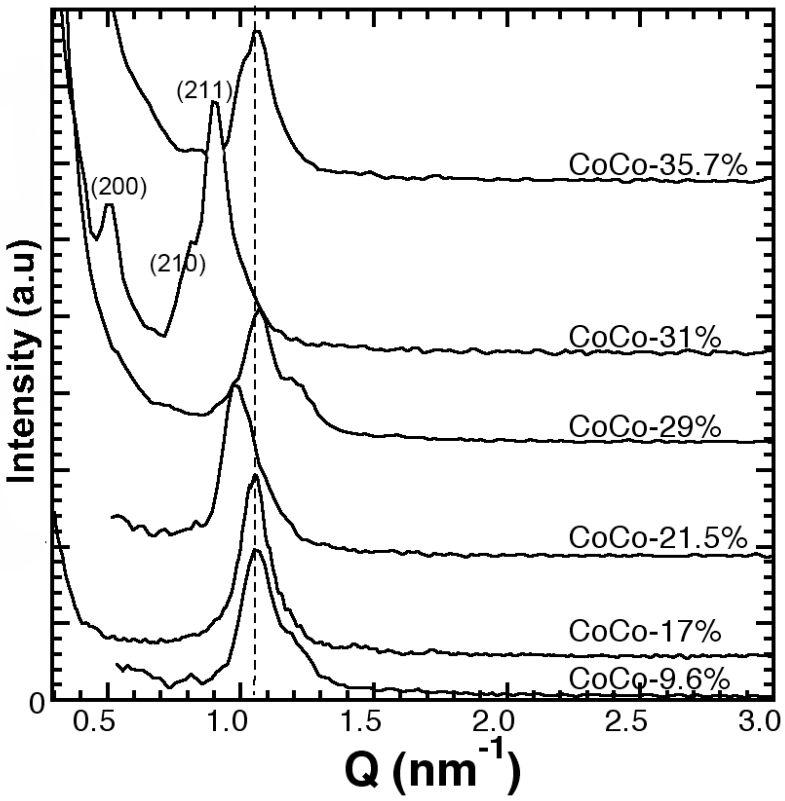

Figure 20. Evolution of the SAXS patterns for CoCo-PBA@MSU prepared with different (PBA/PBA+SiO_2) wt% ratios.

Another explanation of the silica-phase transition has been proposed by Han *et al*.[58] who attributed this phase transition to the effect of nitric acid, and indeed, in these syntheses, the pH is always adjusted to 2 through the use of nitric acid. As the concentration of the $K_3[Co(CN)_6]$ is increased, greater amounts of nitric acid are added to adjust the pH because $K_3[Co(CN)_6]$ is highly basic when dissolved in water (pH = 13). The 35 wt% CoCo-PBA@MSU sample also exhibits a minor ill-ordered bicontinuous cubic-phase. The variations in the final silica structure can be explained based on the aggregation behaviour of the surfactant during evaporation along with the effect of the increased concentration of nitric acid added to the solutions.

3.2.2 Validating CoCo PBA nanoparticle formation inside the matrix

The presence of the $Co_3[Co(CN)_6]_2$ phase inside the mesostructured silica was verified using FTIR (Figure 21). The FTIR analysis of the CoCo-PBA@MSU series confirms the full reaction; however, only a single peak with no shoulder can be observed at 2175 cm-1 (domain of ν(CN)). All peak positions are displayed in Table 4.

Table 4:Infrared bands for MSU-CoCo-PBA@MSU prepared with different concentrations in PBA

Sample	ν (CN) (cm^{-1})	ν(NO_3) (cm^{-1})	δ(OH) (cm^{-1})
MSU-CoCo-9.6%	*2175*	*1386*	*1629*
MSU-CoCo-17%	*2171*	*1385*	*1634*
MSU-CoCo-21.3%	*2173*	*1384*	*1612*
MSU-CoCo-29%	2175	*1384*	*1608*
MSU-CoCo-31%	2175	*1384*	*1610*
MSU-CoCo-35%	*2175*	*1384*	*1611*

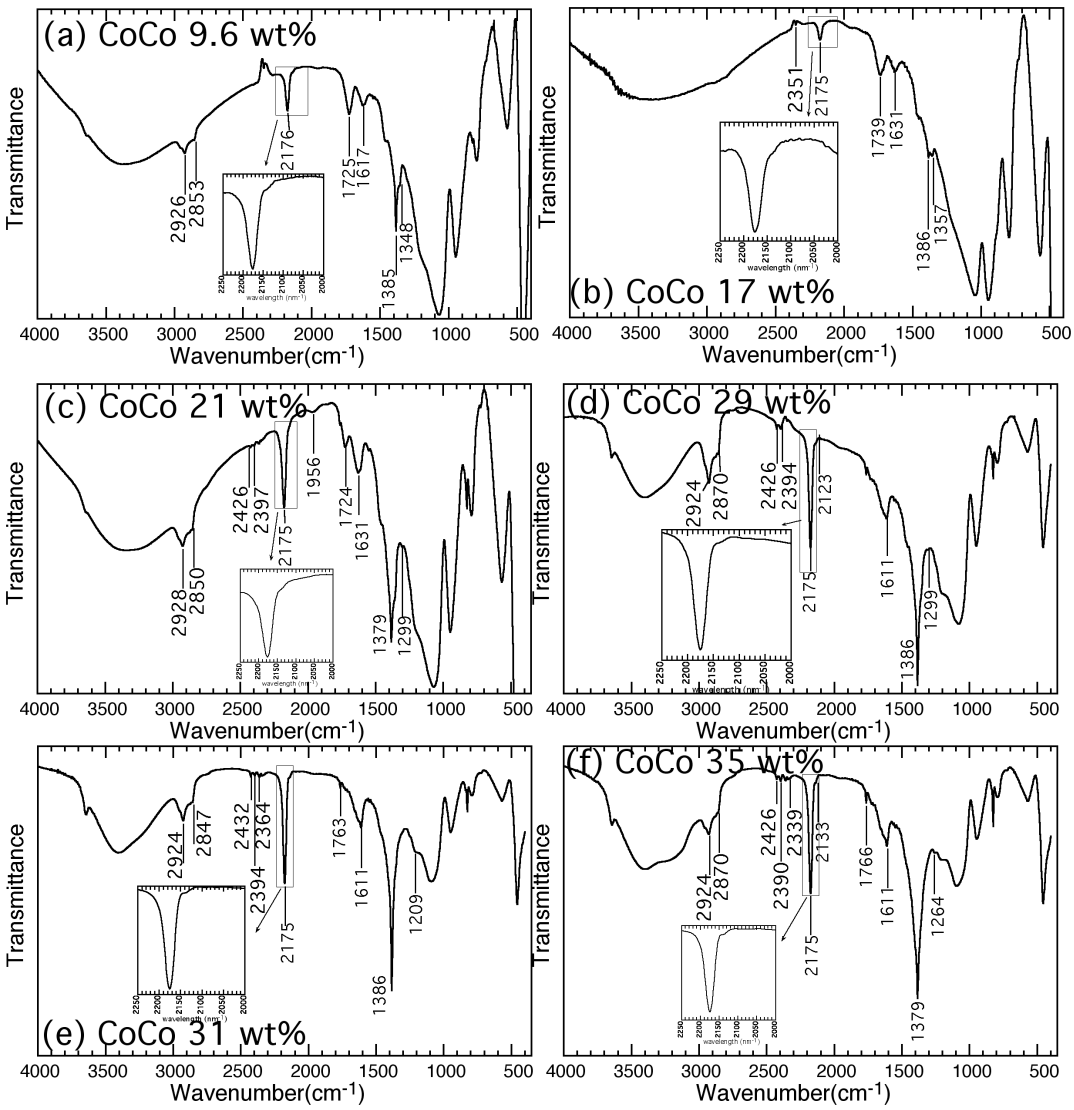

Figure 21. FT-IR spectra of CoCo-PBA@MSU synthesised with higher concentrations in PBA

The presence of a crystalline phase was investigated with the use of XRD diffraction. Powder XRD patterns were recorded for different $Co_3[Co(CN)_6]_2$@MSU samples with the SAXS (over 40°). Figure 22 shows the patterns for all $Co_3[Co(CN)_6]_2$@MSU samples, and a comparison reveals them to be similar to those for the $Ni_3[Co(CN)_6]_2$@MSU samples. All of the diffraction

peaks can be assigned to the fcc structure that would be expected for cobalt hexacyanide.[52, 54] The diffraction patterns are similar, and their intensities tend to increase with additional PBA content.

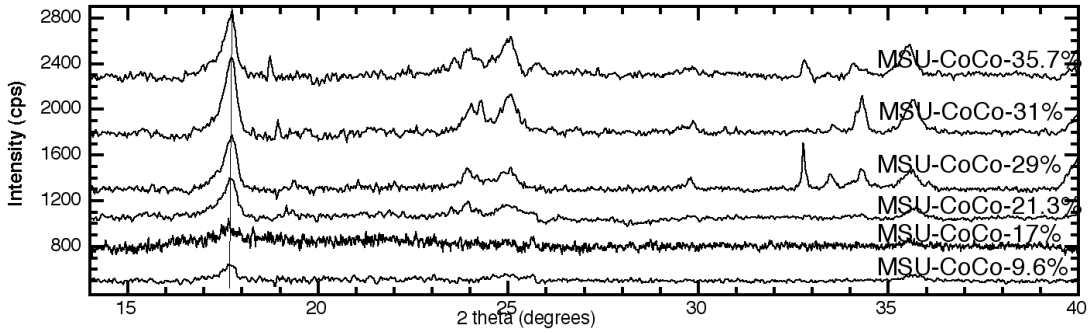

Figure 22. Diffraction patterns for the $Co_3[Co(CN)_6]_2$@MSU samples.

A more accurate analysis was carried out with a dedicated diffractometer for the 29 wt% NiCo and CoCo samples (Figure 23). The diffraction peaks for both $Ni_3[Co(CN)_6]_2$ and $Co_3[Co(CN)_6]_2$, are well identified and Scherrer analysis of the first diffraction peak in each case revealed the presence of 10 nm and 30 nm crystals, respectively.

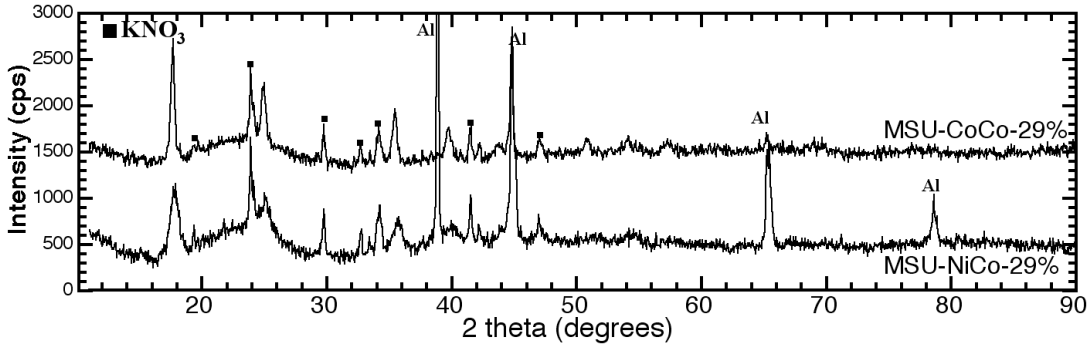

Figure 23. Diffraction patterns for the CoCo(29wt%)-PBA@MSU (top) and NiCo(29wt%)-PBA@MSU (bottom).

The results of this analysis confirm that PBAs can be synthesised within the mesostructured silica matrix at higher quantities than previously reported. As expected, higher concentrations lead to larger crystals: 10 nm and 30 nm for $Ni_3[Co(CN)_6]_2$ and $Co_3[Co(CN)_6]_2$, respectively, in this study rather than 4 nm for $Fe_3[Co(CN)_6]_2$, as observed for low concentrations in previous studies.[52]

3.3 $Sm[Co(CN)_6]$ Synthesis and Analysis

The preparation of $Sm[M(CN)_6].nH_2O$ complexes, with M = Fe, Co as a precursor for different perovskite-type oxides has been studied extensively, mainly with respect to catalytic properties.[59-60] In the work conducted for this thesis, these compounds were used primarily for the preparation of SmCo magnetic alloys. Low-dimensional nanoscale $Sm[M(CN)_6].n\ H_2O$ complexes have been also synthesised with resultant clear changes in their magnetic properties due to changes in size and shape. Sun et al.[61] reported the synthesis of $Sm[Fe(CN)_6].n\ H_2O$ nanoparticles using reverse micelles as soft templates. One focus of the work conducted for this thesis was to prepare a nanoscale $Sm[Co(CN)_6].4\ H_2O$ complex with a uniform size and shape using MSU-silica as a hosting matrix and to study the decompsition of this material through thermal treatment, with the goal of generating nanoscale magnetic alloys. All of the structural parameters of the SmCo PBA samples are displayed in Table 5.

Table 5: Structural Parameters of SmCo-PBA@MSU (PBA Synthesised into 5.9 g / 0.098 mol of SiO_2)

Sample	$Sm(NO_3)_3 \cdot 6H_2O$ (g/*mol*)	$K_3Co(CN)_6$ *(g/mol)*	$[Sm(NO_3)_3 \cdot 6H_2O] / [K_3Co(CN)_6]$ *(mol)*	PBA *(g/mol)*	PBA/(PBA + SiO_2) *wt% / mol %*	d-spacing *nm*
MSU_SmCo- 4%	0.989 g / *2.23 10^{-3}*	0.461 g / *1.3910^{-3}*	1.6	0.25 / *6.95 10^{-4}*	4 / *0.704*	6.2
MSU_SmCo- 8%	1.98 g / *4.45 10^{-3}*	0.922 / *2.77 10^{-3}*	1.6	0.51 / *1.38 10^{-3}*	8 / *1.39*	6.2
MSU_SmCo-11 %	2.97 g/ 6.68 *10^{-3}*	1.38 g/ 4.16 *10^{-3}*	1.6	0.76 /*2.08 10^{-3}*	11.4 / *2.07*	5.7

3.3.1 Influence of SmCo PBA concentration on silica matrix

Figure 24 displays the SAXS pattern of SmCo-PBA@MSU that was prepared with different amounts of PBA, starting with a relatively low concentration because this specific compound had not previously been prepared in MSU -silica. The decision was to begin with a lower concentration followed by sample characterisation in order to validate the presence of SmCo PBAs in the meso-silica matrix. All of the SAXS patterns exhibit one peak around 1 nm^{-1}, a proof of a typical worm-like mesostructured order (the organic templates have not been removed). The SAXS patterns also show no changes in the mesophase as previously reported with higher concentrations of NiCo PBAs and CoCo PBAs.

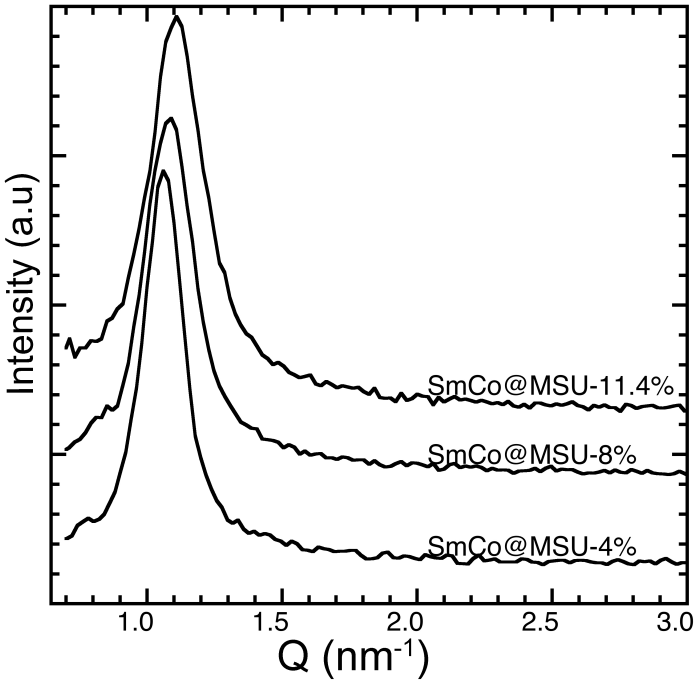

Figure 24. Evolution of the SAXS pattern for SmCo-PBA@MSU prepared with three (PBA/PBA+SiO_2) wt% ratios.

3.3.2 Validating the formation of SmCo PBA nanoparticles inside the matrix

The analysis of the ν(CN) stretching region using FTIR spectroscopy of the SmCo-PBA series (Figure 25 and Table 6) confirms the occurrence of the reaction.[62] showed that there are two characteristic bands for the $C \equiv N$ stretching in $Ln[Fe(CN)_6].4\ H_2O$ complexes. They proved that these two bands shift slightly toward higher frequencies as the Ln^{+3} radius increases, which slight changes have been attributed solely to variations in Ln. FTIR spectra for the $Sm[Co(CN)_6]$-MSU samples show a strong band at 2162 cm^{-1} and a weaker band at 2150 cm^{-1}, which can be attributed to the $C \equiv N$ stretching bands.

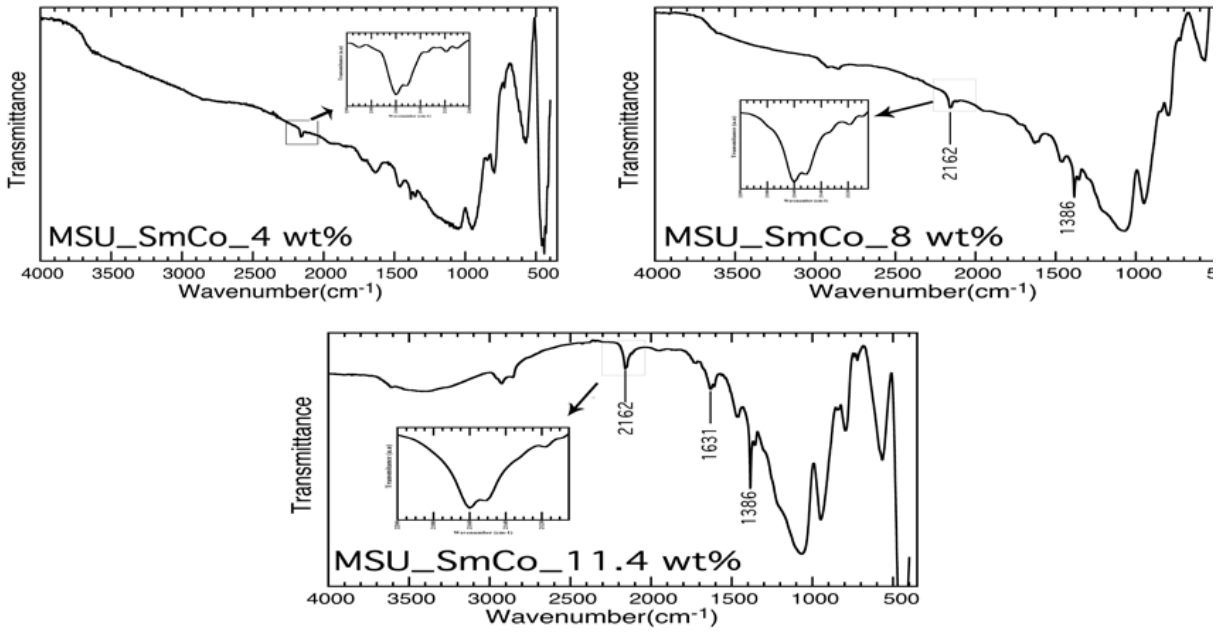

Figure 25. FTIR spectra of SmCo-PBA@MSU synthesized with different concentrations of PBAs (inset: domain of ν(CN)).

Table 6: Infrared bands for MSU-SmCo-PBA@MSU prepared with different concentrations in PBA

Sample	ν (CN) *(cm^{-1})*	ν(NO_3) *(cm^{-1})*	δ(OH) *(cm^{-1})*
MSU-SmCo- 4%	*2160 + 2150*	*1389*	*1637*
MSU-SmCo- 8%	*2160 + 2150*	*1384*	*1631*
MSU-SmCo- 11%	*2160 + 2150*	*1386*	*1631*

The powder XRD results for the $Sm[Co(CN)_6]$-MSU series are shown in Figure 26 and were derived from tests carried out with a dedicated diffractometer. The diffraction pattern that can be observed is attributable to the $Sm[Co(CN)_6].4\ H_2O$.[63]

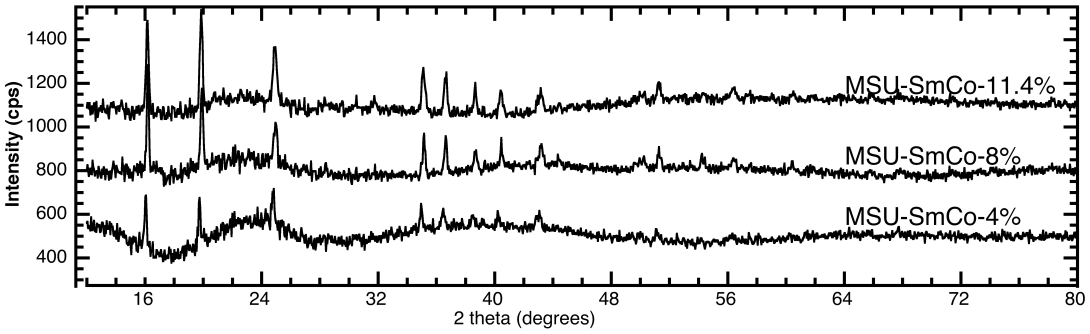

Figure 26. Diffraction pattern for the $Sm[Co(CN)_6]$@MSU samples.

All of the diffraction patterns are similar, and their intensities increase with additional SmCo PBA content. The nanoparticle size that was estimated based on the diffraction using the Scherrer formula ranged from 30 nm for SmCo 4 wt% to 45 nm for SmCo 11 wt%.

Chapter 4

Thermal Evolution of PBAs in MSU and Their Magnetic Properties

4.1 Thermal Evolution and Magnetic Properties of NiCo PBAs

4.1.1 NiCo PBAs thermally treated in air

Thermal treatment of the NiCo(35wt%)-PBA@MSU was followed by temperature-programmed XRD (TP-XRD) in air (Figure 27) or helium (Figure 32), the samples being left at each temperature for 10 min prior to data recording.

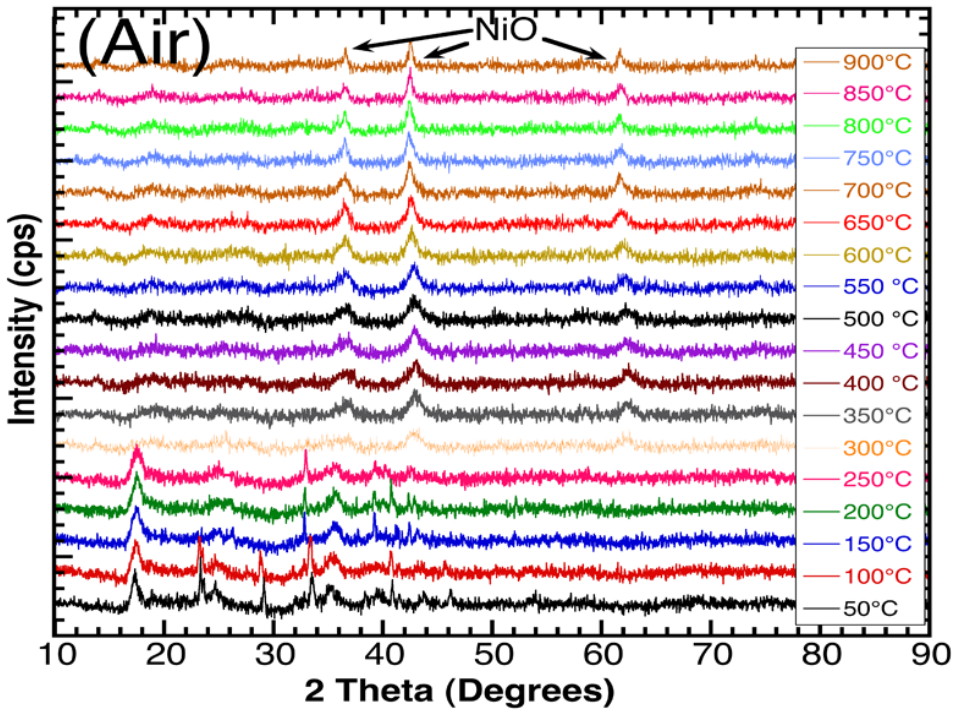

Figure 27. TP-XRD of the NiCo(35 wt%)-PBA@MSU in air.

The initial PBA *fcc* structure is preserved up to 250 °C. Above 300 °C, the sample in air begins to decompose (Figure 27), and a new diffraction pattern appears, with three broad peaks at 36 degrees, 42.5 degrees, and 62 degrees, corresponding to the (*111*), (*200*), and (*220*) planes

of NiO, respectively.[64] These peaks narrow with increased temperature, however they remain rather broad, even at 900°C.

The influence of the thermal treatment was studied further by annealing the samples at 600°C for 4 h in air. This treatment was first applied to the NiCo-PBA@MSU series. Figure 28 displays the XRD pattern of these materials after a 4 h thermal treatment at 600 °C.

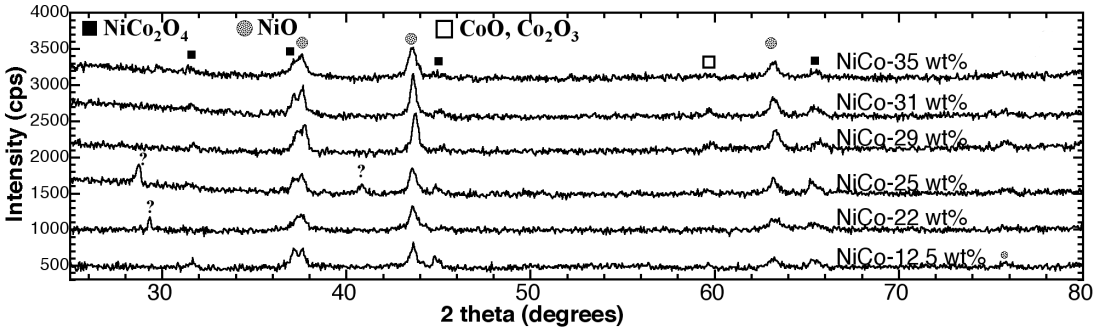

Figure 28. XRD patterns of the NiCo-PBA@MSU series calcined at 600 °C for 4 h in air.

For all samples, the two major phases obtained were nickel oxide and the spinel $NiCo_2O_4$ (with a small fraction of cobalt oxide). These results demonstrate that the spinel $NiCo_2O_4$ phase can be obtained inside the silica matrix, from the initial NiCo PBA, by thermal decomposition. This phase is thermally unstable, and nanoparticles alone begin to decompose at 400 °C, to produce nickel oxide.[65] The formation of the pure $NiCo_2O_4$ spinel primarily at a low calcination temperature (375°C) and the initial 1.5 nickel:cobalt ratio explain the formation of the NiO phase in parallel; it is clear that at a higher temperature, $NiCo_2O_4$ decomposes, yielding an NiO impurity.[65] This route of the synthesis of $NiCo_2O_4$ suggests that the problems related to structural instability inherent in other approaches can be overcome because $NiCo_2O_4$ has been successfully

synthesised even at a 600°C calcination temperature. The presence of $NiCo_2O_4$ nanoparticles was confirmed using TEM analysis, as shown in Figure 29.

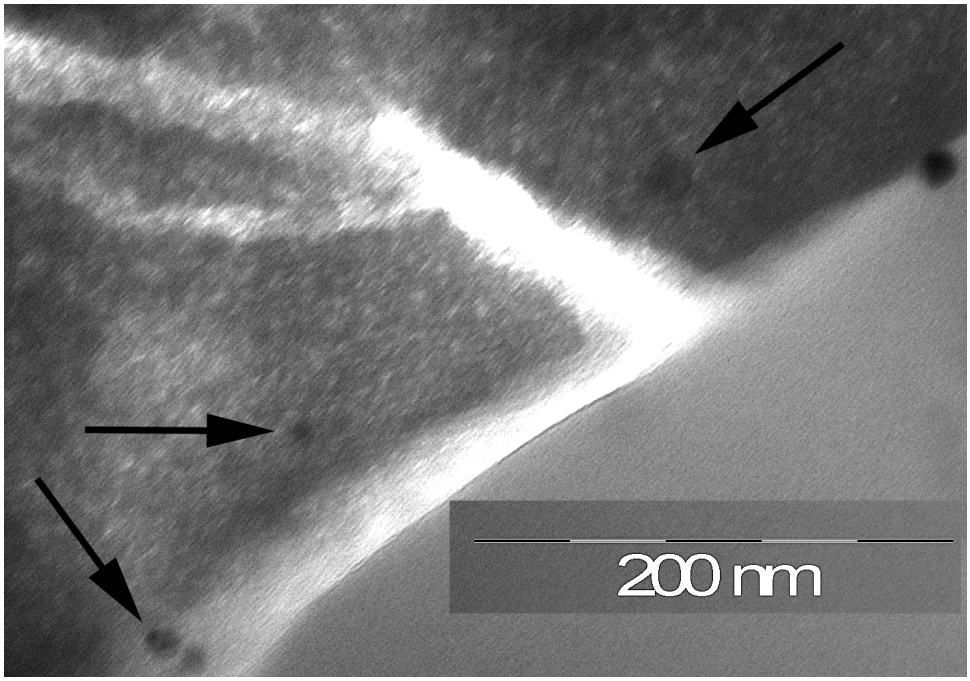

Figure 29. TEM observation of the 12.5 wt% NiCo-PBA@MSU, after 600 °C calcination in air. The arrows depict the 20 nm $NiCo_2O_4$ oxide nanoparticles.

This analysis confirms that 20 nm $NiCo_2O_4$ nanoparticles have been obtained as isolated nanoparticles embedded in the silica host matrix.

4.1.2 Magnetic characterization

Samples treated in air were identified to be NiO/$NiCo_2O_4$/silica nanocomposites. Given the ferrimagnetic ($NiCo_2O_4$), antiferromagnetic (NiO), and diamagnetic (the silica matrix) character of the nanocomposites, the magnetic behaviour cannot be attributed to a single phase. NiO bulk crystals are known to be antiferromagnetic, with the 523 K being a Neel temperature, it has been demonstrated, however, that when the particles sizes reduced to the order of a few nanometers,

the NiO nanoparticles exhibit superparamagnetic or superantiferromagnetic behaviour that increases as the dimension of the particles decreases .[66] Bulk $NiCo_2O_4$, on the other hand, is a ferrimagnet with a Curie temperature being about 400 C.[67]

The magnetic measurement at 300 k for the 12.5 wt% sample are displayed in Figure 30 (a), and the figure indicates a magnetic behaviour that can be attributed to the finite size effects of NiO.[68] It can be seen that no hysteresis is observed at room temperature, a feature that is characteristic of both a spin-glass and a superparamagnet system. For the 12.5 wt% sample, the loops are rather narrow, and shifted from the origin, this feature is one of the defining characteristics of the spin-glass behavior.[69] In contrast, Figure 30 (b) shows the magnetic measurement at 300 k for the 35 wt% sample. Although this measurement also reveals no hysteresis at room temperature, the loops are identical and symmetric around the centre, an effect that is attributable primarily to superparamagnetic behaviour.[70]

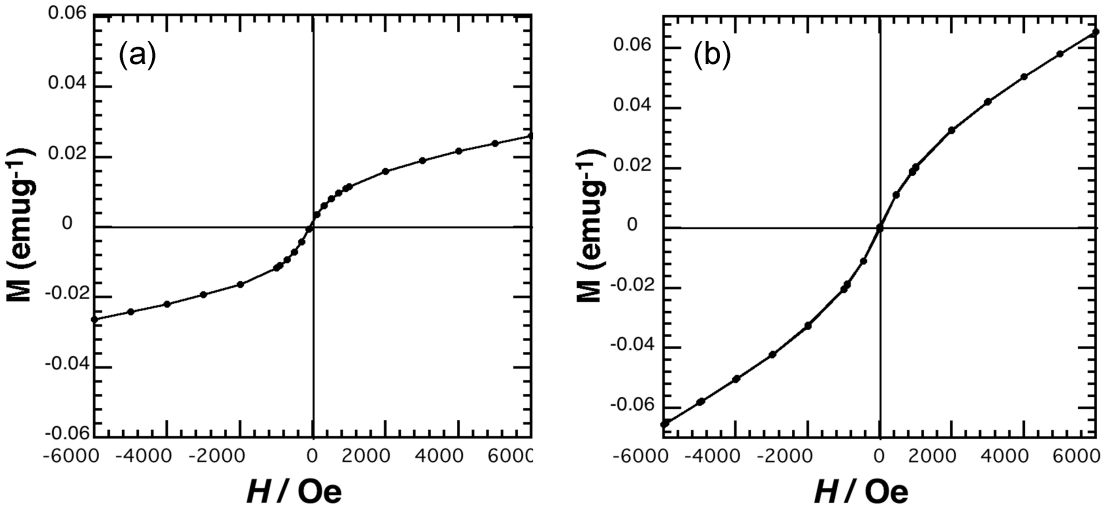

Figure 30. Magnetization of (a) NiCo/12.5wt%@MSU and (b) NiCo/35wt%@MSU after thermal treatment in air, measured at 300 K.

The magnetic properties of these samples were studied further using a SQUID magnetometer. The measurements for these samples were taken well below their glass transition or blocking temperature, specifically at 2.5 K. The hysteresis loops are shown in Figure 31. The coercive field was measured to be approximately 430 Oe for the 12.5 wt% sample and 1160 Oe for the NiCo 35 wt% sample (Figures 31(a) and 31(b), respectively). The decrease in magnetization (M) for the 35%NiCo sample can be assigned to the segregation of the antiferromagnetic NiO phase. [71] There is an increase in the coercive value from 430 Oe for the 12.5 wt% sample to a value of 1160 Oe for the 35 wt% sample, which could be attributed to the pinning effect that was introduced mainly by the NiO phase.[72] Especially for the NiCo 35 wt% sample, this magnetic characterization indicates that the thermally treated nanocomposite holds relatively the same magnetic properties as the pure spinel $NiCo_2O_4$, as reported by Verma *et al*.[65]

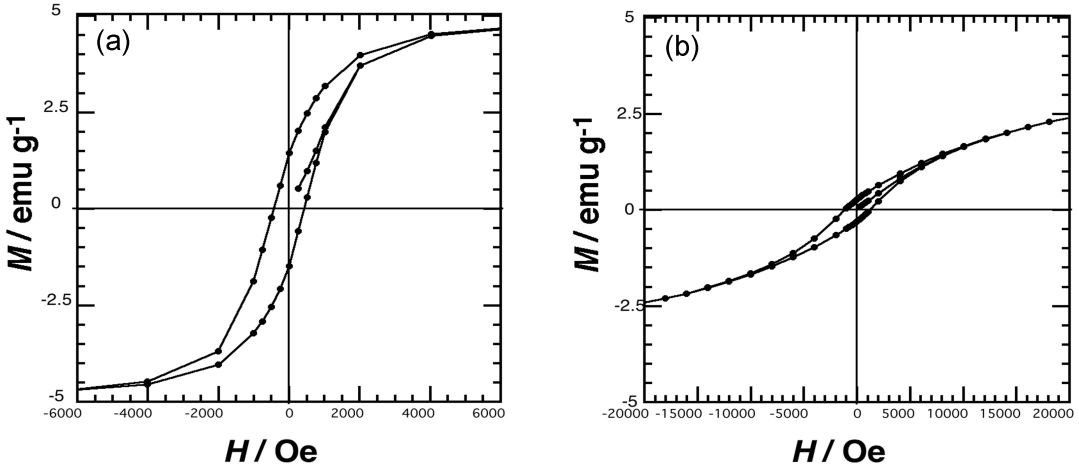

Figure 31. Magnetization of (a) NiCo/12.5wt%@MSU and (b) NiCo/35 wt %@MSU after thermal treatment in air, measured at 2.5 K.

4.1.3 NiCo PBAs thermally treated in a neutral atmosphere

At high temperatures, the sample treated in helium (Figure 32) exhibits the diffraction peaks of the *fcc* NiCo alloy, peaking out at 44.0 (*111*), 51.3 (*200*), and 75.4 (*220*) degrees.[73]

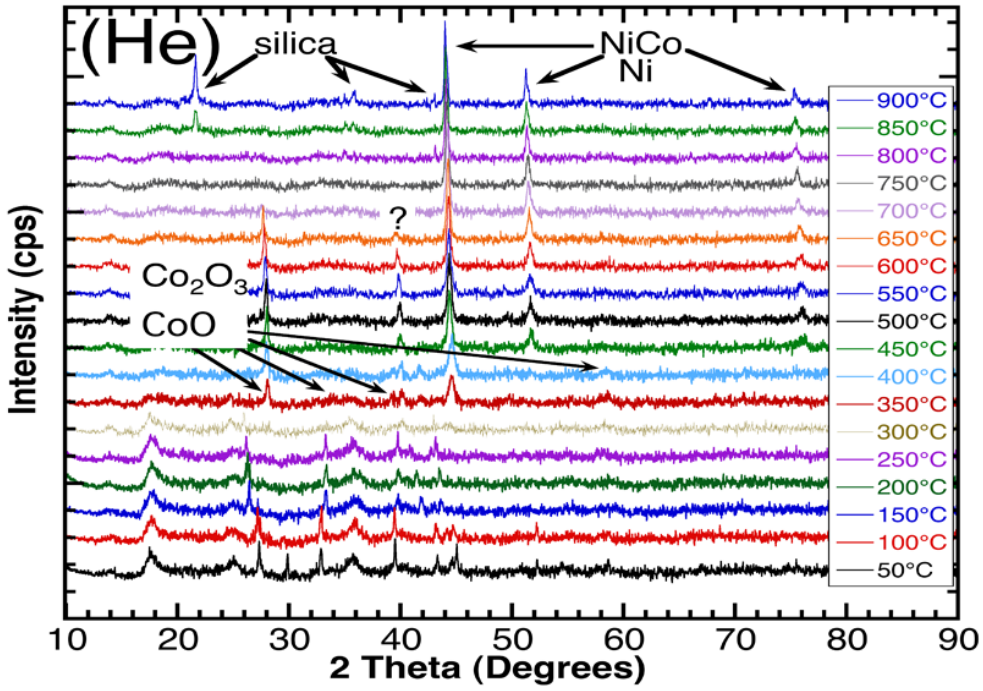

Figure 32. TP-XRD of NiCo(35 wt%)-PBA@MSU in He.

Thermal treatment in a neutral atmosphere (Figure 32) leads to a different evolution. From room temperature to 300°C, the same collapse of the initial phase can be observed, followed by the intermediate formation of cobalt oxide (possibly Co_2O_3 or CoO), that then disappears at 600°C. In parallel, the formation of reduced metal (diffraction peaks can be assigned indifferently to Ni or NiCo) begins at 350°C. This reduction at a rather low temperature cannot be explained by the spontaneous reduction of nickel oxide because the oxidation reaction is quite endothermic (-400 kJ/mol) and proceeds usually with a very low partial pressure of oxygen. This

quick reduction can therefore be explained based on a combination of two factors: the very small size of the initial PBA nanoparticles and their insertion into the initial organic matrix composed of surfactants, whose calcination enhances the local reducing atmosphere. Finally, a remaining diffraction peak at 40 degrees can be observed between 300°C and 650°C, which proved to be too difficult to assign . The influence of the thermal treatment was studied further through the annealing of the samples at 600 °C for 4 h in argon (Figure 33).

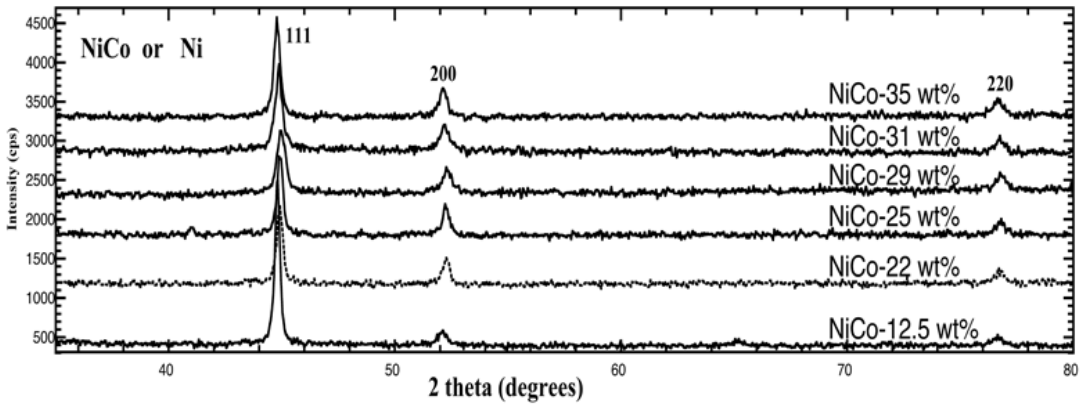

Figure 33. XRD patterns of the NiCo-PBA@MSU series calcined at 600 °C for 4 h in Ar.

Heating the samples at 600 °C for 4 h in Ar leads to a metallic phase, created as a result of the non-oxidising atmosphere and the internal reduction caused by the organic combustion.

4.1.4 Magnetic characterization

The measurements of the magnetization as a function of the strength of the applied magnetic field at 300 K for the NiCo 22 wt% and NiCo 35 wt% samples thermally treated in argon are displayed in Figures 34 (a) and 34 (b), respectively.

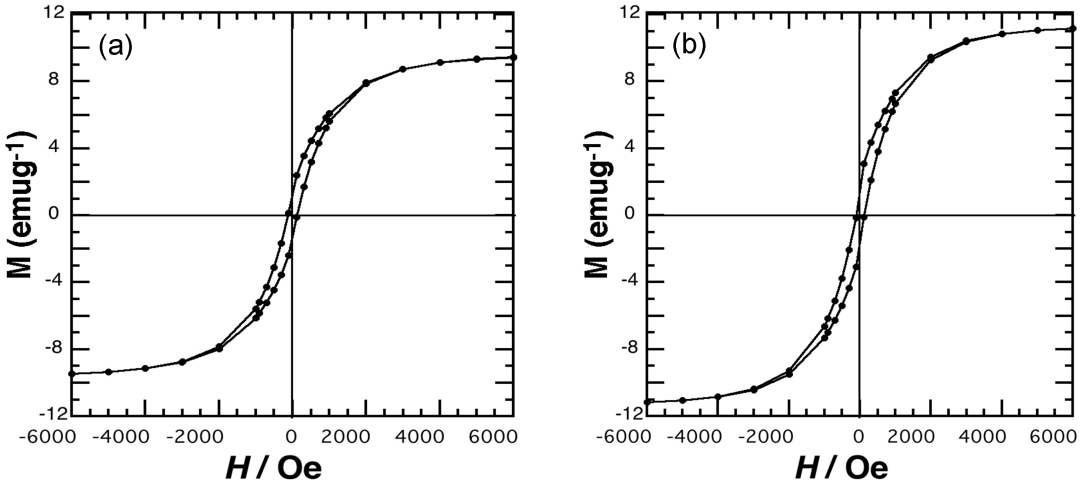

Figure 34. Magnetization of (a) NiCo/22wt%@MSU and (b) NiCo 35% @MSU after thermal treatment in Ar, measured at 300 K.

These nanocomposites are magnetic at room temperature and can be easily manipulated using a regular magnet. Figure 34 shows the M-H loops obtained at 300 K and reveals an open hysteric behaviour that reaches a magnitude of 9.5 emu.g^{-1} for the NiCo 22 wt% sample. The coercive field was measured at approximately 145 Oe. The sample with the higher concentration, namely the NiCo 35 wt% sample, shows an open hysteresis loop that reaches a higher magnetization at 11 emu.g^{-1}, with a coercive field measured at approximately 126 Oe for this sample.

4.2 Thermal Evolution and Magnetic Properties of CoCo PBAs

4.2.1 CoCo PBAs thermally treated in air

For the CoCo PBAs system, the same thermal treatment was applied as with the NiCo system, and similar behaviour was observed for the CoCo-PBA@MSU samples. When the sample was calcined in air at 600 °C for 4 h, a pure Co_3O_4 spinel oxide phase was obtained, and no other phases or impurities were observed (Figure 35).

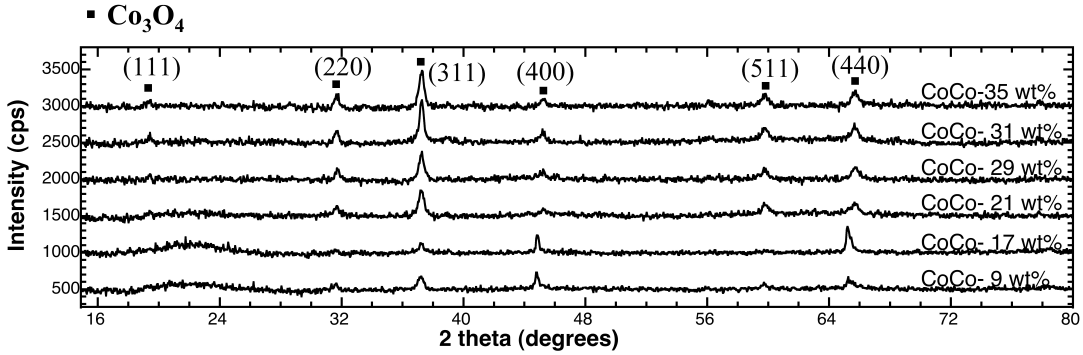

Figure 35. XRD pattern of CoCo-PBA@MSU samples prepared with different amounts by wt% of the PBA, calcined at 600 °C in air.

Figure 35 shows broadened diffraction peaks, which suggest that this spinel Co_3O_4 oxide was crystallised within the silica mesostructure framework through the confinement process. The mean size of the nanoparticles was estimated from the diffraction using the Scherrer formula (Equation 6) to be in the range of 15 nm for the CoCo 9 wt% to the size of 20 nm for the CoCo 35wt%.

$$L = \frac{0.89 * \lambda}{B * \cos\theta} \qquad (6)$$

where L = the average crystal size and B = the full width of half the maximum of the peak. All of the diffraction peaks can be assigned to the *fcc* structure that was expected for the Co_3O_4.[74] The diffraction patterns are all similar, and their intensities tend to increased with additional PBA content.

4.2.2 Magnetic characterization

Co_3O_4 bulk crystals are known to be antiferromagnetic, with the 30 K being the Neel temperature.[75] A typical response of an antiferromagnetic material is that when a magnetic field is applied, the magnetization increases almost linearly.. However, in the CoCo 35wt% sample, and despite the anti-ferromagnetic character of the Co_3O_4, and the diamagnetic character of the silica matrix, ferromagnetic behaviour was observed at 300 k for this sample.

The Co_3O_4 nanoparticles synthesised within the MSU silica also exhibited interesting magnetic properties that were not expected for this phase of the oxide, as shown in (Figure 36).

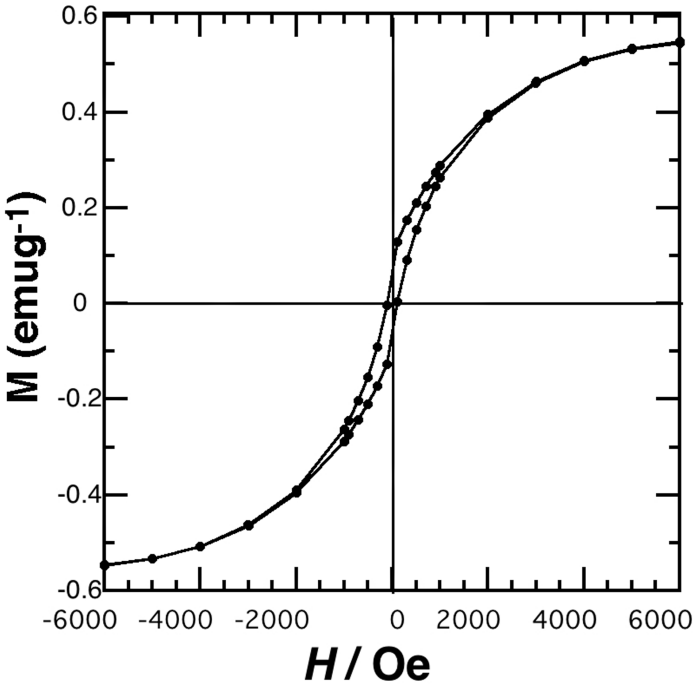

Figure 36. Magnetization of CoCo/35wt%@MSU after thermal treatment in air at 600 ºC for 4 h, measured at 300 K.

The magnetic measurements for the CoCo 35wt% sample, thermally treated in air at 600 ºC for 4 h, reveal an open hysteric behaviour that reaches a magnitude of 0.55 emu.g^{-1} and a coercive field of approximately 96 Oe. It has been reported, however, that similar results were obtained using mixtures of TiO_2 and Co_3O_4.[76]

4.2.3 CoCo PBAs thermally treated in a neutral atmosphere

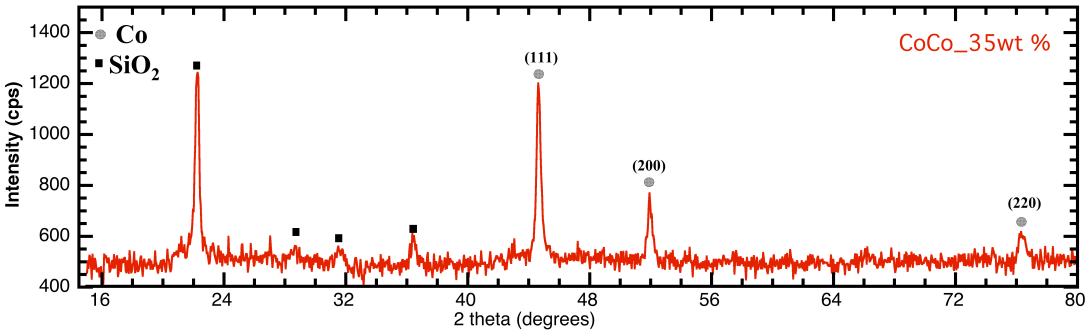

Figure 37. XRD pattern of three CoCo-35wt %@MSU samples calcined at 900 ºC for 4 h in Ar.

Figure 37 shows a typical XRD pattern for the Co nanoparticles as a result of annealing the CoCo 35wt% sample in Ar at 900 ºC for 4 h. This pattern can be indexed to a pure *fcc* cobalt phase,[77] with no indication of cobalt oxide, and the other peaks shown in the graph are related to the SiO_2 crystalline phase. These Co nanoparticles have an average diameter of 24 nm, calculated using the Scherrer formula.

4.2.4 Magnetic characterization

Cobalt nanoparticles are known to have magnetic properties with high magnetocrystalline anisotropy, [78] which make them very good candidates for high-density recording media. Figure

38 displays the magnetisation behaviour of the Co-nanoparticles obtained after thermal treatment of the CoCo 35 wt% sample in Ar at 900 ºC for 4 h. The magnetic measurement revealed an open hysteric behaviour that reaches a magnitude of 19 emu.g^{-1} and a coercive field measured at approximately 90 Oe at 300 K, as shown in Figure 38 (a). A measurement was also obtained at 100 K for the same sample and revealed an increase in the coercive field that reaches a magnitude of 145 Oe, as shown in Figure 38 (b).

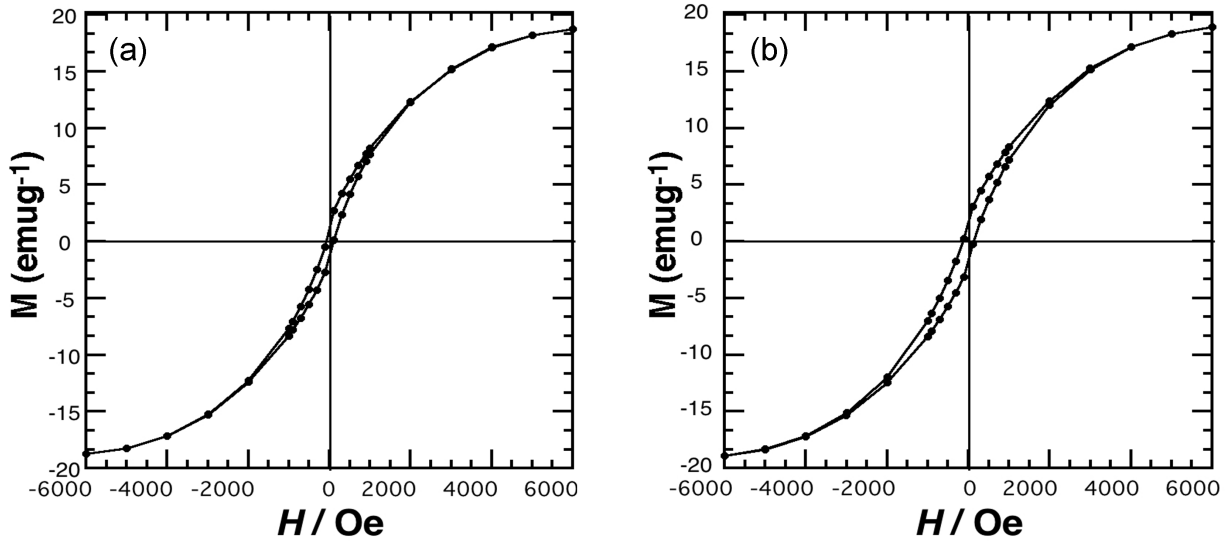

Figure 38. Magnetization of the samples thermally treated in Ar at 900 ºC for 4 h: (a) CoCo/35wt%@MSU measured at 300 K and (b) CoCo/35wt%@MSU measured at 100 K.

4.3 Thermal Evolution and Magnetic Properties of SmCo PBAs

4.3.1 SmCo PBAs thermally treated in a neutral atmosphere

Several thermal treatments at different temperatures were applied to the SmCo/4wt%@MSU sample, from 600 ºC to 900 ºC. It is worth noting that at up to 800 ºC, this sample showed no crystalline peaks except the silica peaks; however, when the sample was annealed at 900 ºC for 4

h, small broad peaks started to appear on the diffraction pattern, indicating the formation of a crystalline phase, as shown in Figure 39. Most of these peaks correspond to the $SmCo_3$ crystalline phase.[79]

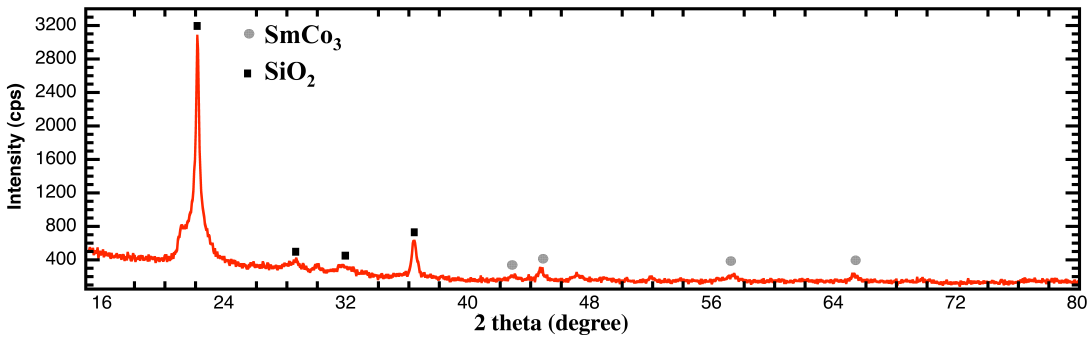

Figure 39. XRD pattern of three SmCo-4 wt %@MSU samples calcined at 900 ºC for 4 h in Ar.

As estimated by Scherrer formula using the XRD diffraction pattern, the average particle size of the $SmCo_3$ is approximately 9 nm. The XRD pattern reveals that the final product contains more than just a single phase because of the presence of some unidentified peaks that are evidence of the introduction of impurities into the $SmCo_3$.

4.3.2 Magnetic characterization

Figure 40 presents the magnetization loops for the materials obtained. Superparamagnetic behaviour can be observed at room temperature for this sample, with an unsaturated loop even at 15,000 Oe, indicating a combination of superparamagnetic and ferromagnetic behaviour.[80]

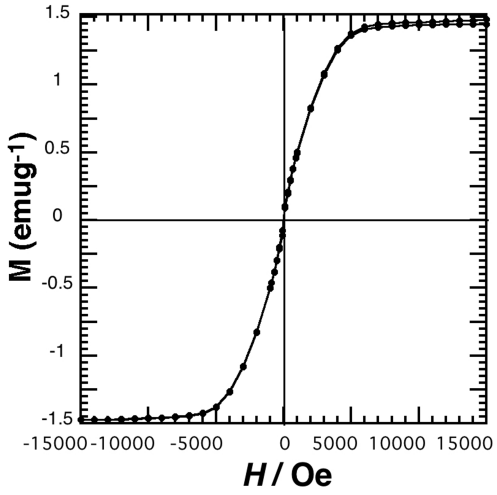

Figure 40. Magnetization curves measured at 300 K for the SmCo/4wt %@MSU sample thermally treated in Ar for 4h at 900 ºC.

The sample with the higher SmCo PBA content, namely SmCo 11.4 wt%, thermally treated at 800ºC for 5 h, exhibits ferromagnetic behaviour at room temperature (Figure 41), and it shows hysteresis at room temperature with a low coercive field of about 120 Oe. When the magnetic properties were measured at 100 K, the coercivity increased to reach 211 Oe, and the hysteresis loop also increased.

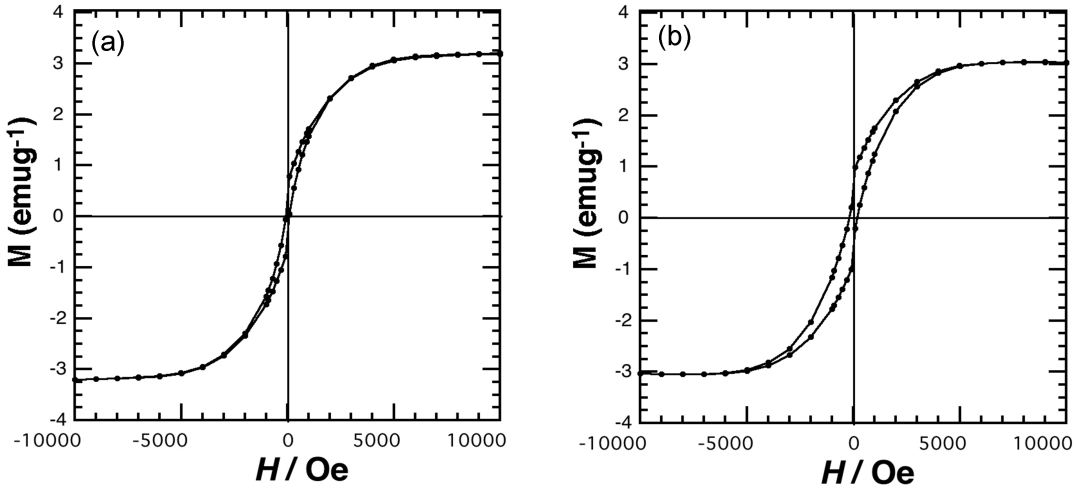

Figure 41. Magnetization curves for the SmCo/11 wt%@MSU sample thermally treated in Ar for 5 h at 800 ºC, (a) measured at 300 K and (b) measured at 100 K.

The XRD pattern, however, showed very small and broad peaks that could not be clearly assigned to one distinct SmCo alloy phase. Figure 42 shows the XRD pattern for the SmCo-11 wt %@MSU sample calcined at 800 ºC for 5 h in Ar. While it is clear that even at this relatively high temperature, the silica did not crystallize, it is not apparent whether the higher SmCo content has a direct effect on silica crystallization. The $SmCo_3$ alloy phase, however, can be identified as shown in the figure, but the magnetic properties cannot be assigned to one single phase, and further investigation of this thermal treatment should be conducted, perhaps for a longer time or at a higher temperature.

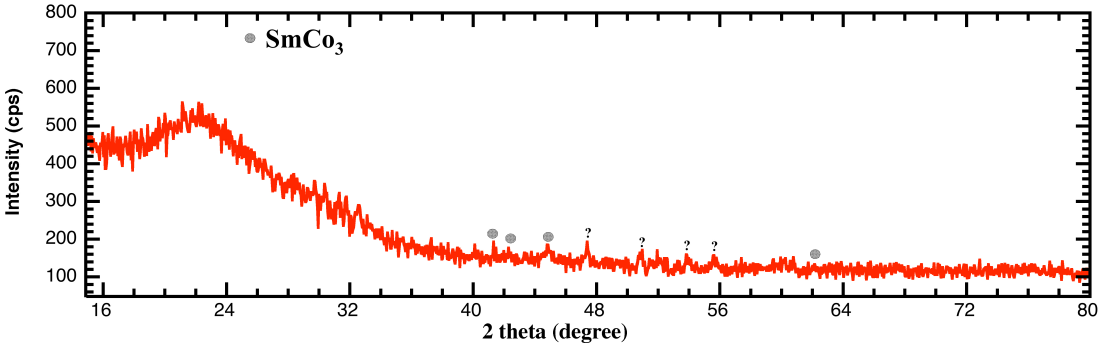

Figure 42. XRD pattern for the SmCo-11 wt %@MSU sample calcined at 800 ºC for 5 h in Ar.

Chapter 5

Non-Conventional Heating Methods

5.1 Microwave irradiation

One of the most important advantages of using non-conventional heating methods for chemical synthesis, such as microwave irradiation, is the substantial reduction in the overall reaction time, as well as the possible creation of new phases. Based on well-defined mechanisms and parameters, the extensive use of microwave irradiation has generally resulted in significant improvements with respect to organic synthesis . It has been reported, however, that for solid-state inorganic materials , the mechanism that allows the coupling of the microwave irradiation to the materials and the subsequent energy dissipation out of the materials can be rather complex. [81]

For this thesis work , the NiCo 31wt% sample was used in order to test the application of microwave irradiation at 600 W for 15 min. These experiments were preliminary tests to evaluate if such a way should be explored in the future. The result for this sample was a complete collapse of the meso-silica structure, as shown in Figure 43. As this treatment involves the addition of DI water (20 ml) as a solvent, one may deduce that the silica does not resist to the resulting hydrothermal conditions. Unlike silica, the PBA structure was preserved and improved, with a clear increase in the peak intensities, as shown in the XRD analysis depicted in Figure 44. Compared to the as-synthesized sample, all peaks have been preserved; however, all by-products that were present on the as-synthesized sample disappeared after the microwave treatment.

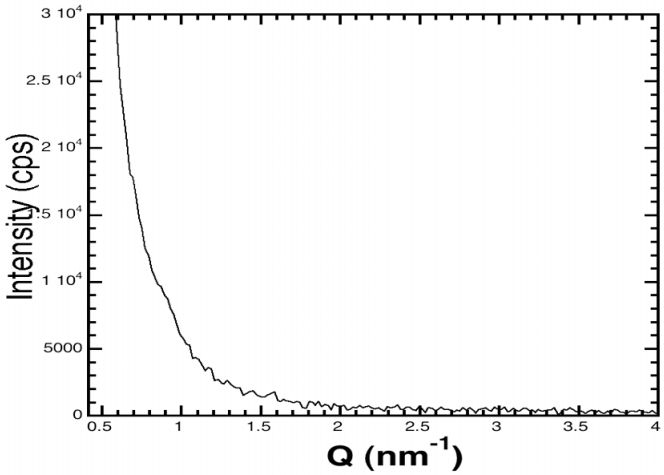

Figure 43. SAXS pattern for the NiCo 31 wt% @MSU sample treated with microwave irradiation at 600 W for 15 min.

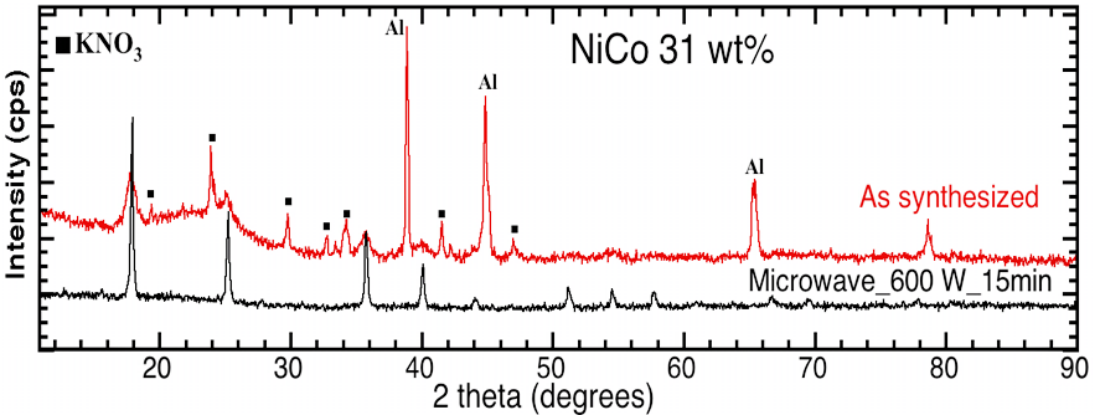

Figure 44. Diffraction patterns for NiCo 31 wt% @MSU samples: as-synthesized and treated with microwave irradiation at 600 W for 15 min.

Scherrer analysis of the first diffraction peak revealed the presence of 10 nm crystals for the as-synthesized sample and 15 nm crystals for the microwave-treated sample.

Vondrova *et al.*[82] reported that microwave irradiation of Prussian blue analogues (PBAs) leads to a significant increase in the mixture temperature, which causes the reduction of the metal centres to form transition metal alloys in a few minutes rather than several hours, as required

with conventional furnace heating.[82] SmCo samples were treated at a higher frequency (1100 W for 4 minutes), and we used a strong microwave absorbent (ethanol, 20 ml). Diffraction reveals that the silica structure remains unchanged (Figure 45). When a very strong absorbent such as ethylene glycol (20 ml) is used, however, the meso-silica structure collapses completely.

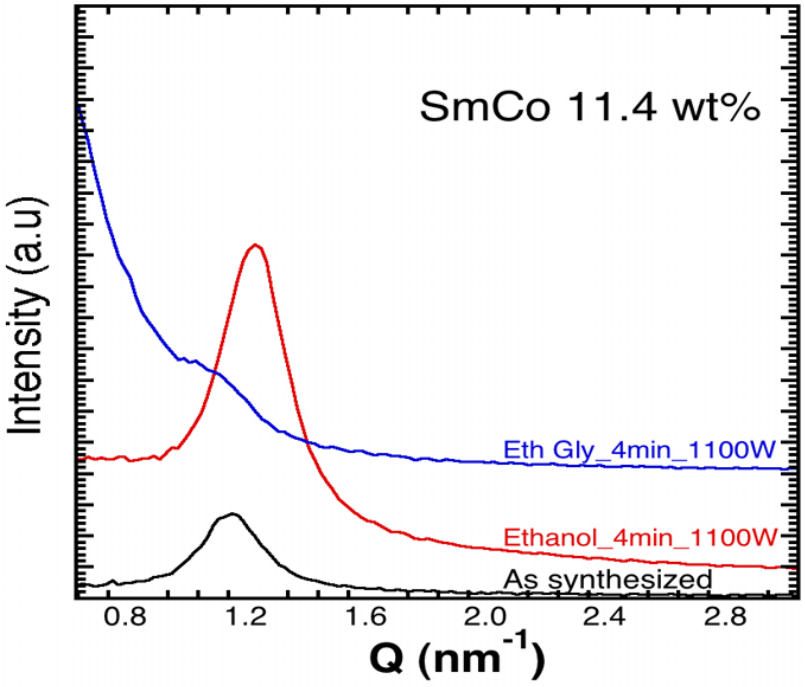

Figure 45. SAXS pattern for the SmCo 11.4 wt% @MSU sample treated with microwave irradiation at 1100 W for 4 min using different solvents.

The SmCo PBA structure shows a slight shift on the XRD pattern to a lower 2Θ value, as displayed in Figure 46. This shift can be attributed to complete dehydration and the complete removal of H_2O from the structure: the microwave irradiation causes a dehydration of the pristine PBA compound, leading from $Sm[Co(CN)_6].4\ H_2O$ to $Sm[Co(CN)_6]$, as confirmed by XRD analysis.

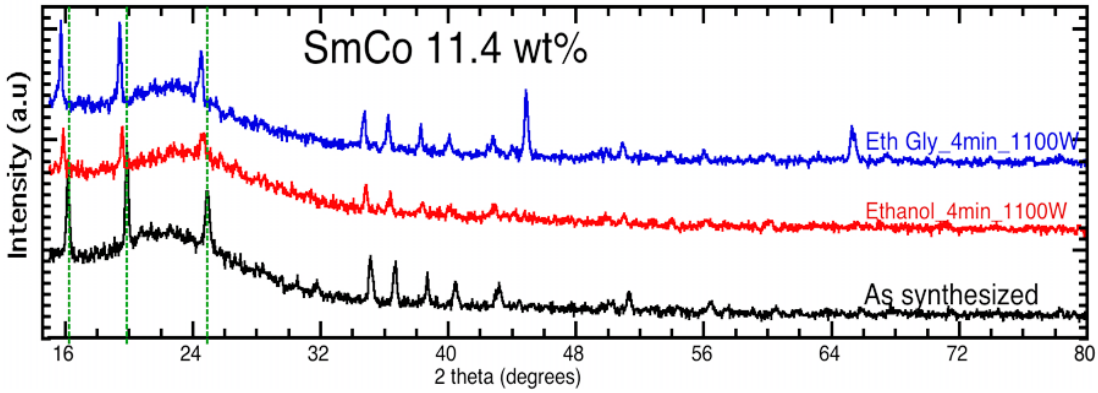

Figure 46. Diffraction patterns for the SmCo 11.4 wt% @MSU samples: as-synthesized and treated with microwave irradiation at 1100 W for 4 min using different solvents.

The same treatment was applied to the SmCo 8wt%@MSU, with the same results (Figures 47 and Figures 48).

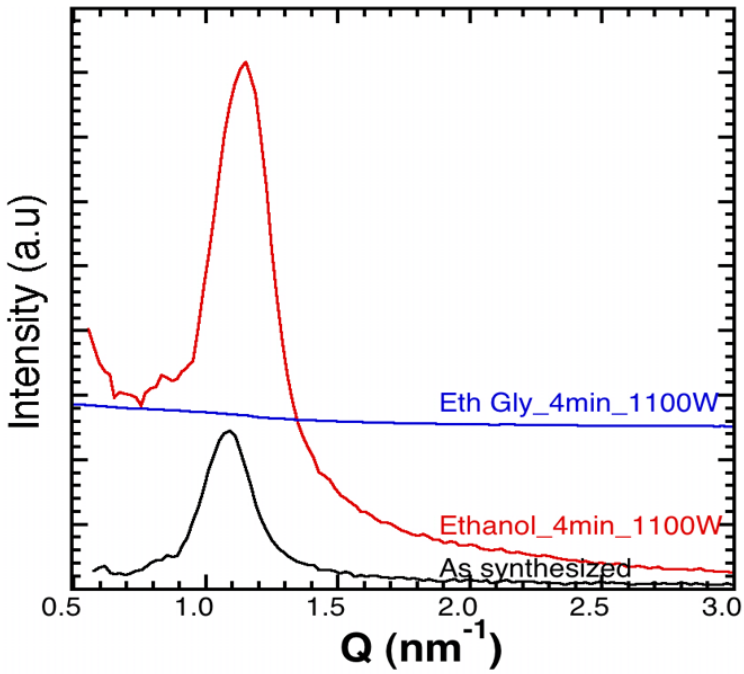

Figure 47. SAXS pattern of the for the SmCo 8 wt% @MSU sample treated under microwave at 1100 W for 4 min using different solvent.

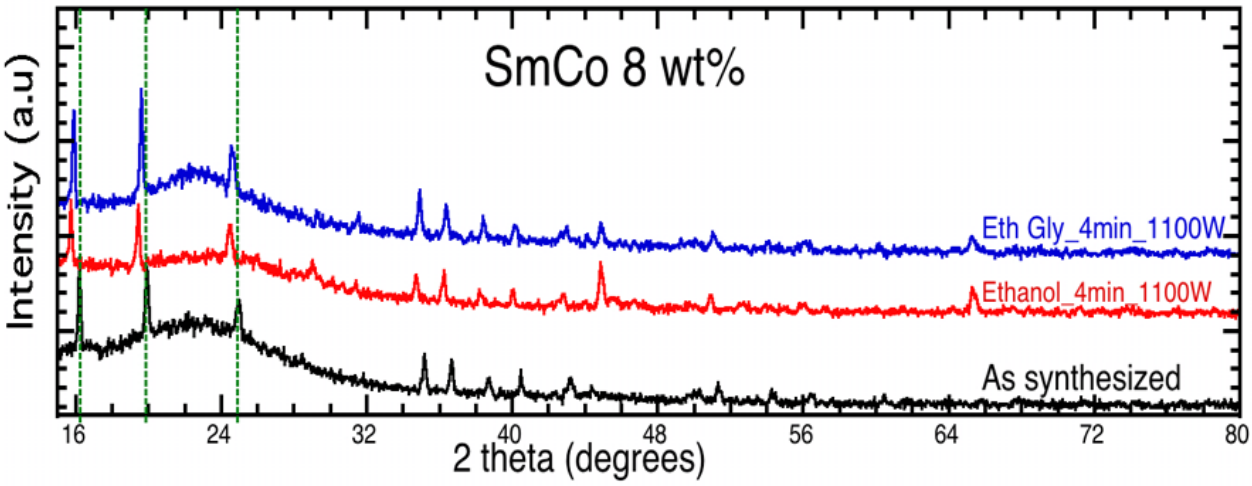

Figure 48. Diffraction pattern of the for the SmCo 8 wt% @MSU sample as synthesizes and treated under microwave at 1100 W for 4 min using different solvents.

These results, obtained under different conditions, clearly indicate that different parameters, such as sample type, frequency, solvent, and sample concentration, can have a dramatic effect on the final product.

Metal alloys, however, were not produced using microwave irradiation, a result that can be attributed to the use of a silica matrix in the synthesis for this research: the silica matrix appears to absorb a significant amount of the microwave irradiation, which leads to the complete collapse of the mesostructure, and hence, no significant changes can be observed in the PBA structure compared to those reported for bulk PBAs.

The Microwave treatment was performed with a Synthos 3000 microwave reaction system (Anton Paar) that can operate with 1400 W un-pulsed microwave output from two magnetrons.

5.2 UV treatment

The NiCo 35 wt%@ MSU sample was used in order to test the application of a UV treatment both in air and in nitrogen for 30 min: the SAXS analysis results are displayed in Figure 49. The meso-silica structure has been preserved with a clear shift of the peaks toward a higher q value, indicating some changes in pore configuration. In the nitrogen atmosphere, however, the peaks are enhanced, and the intensity is increased.

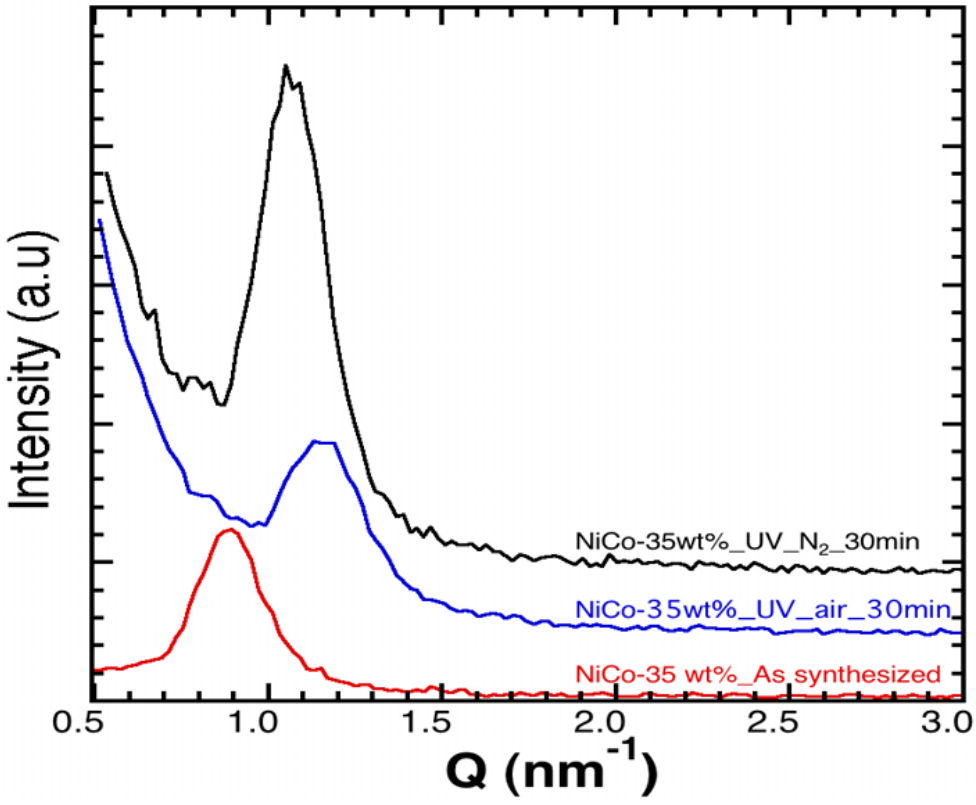

Figure 49. SAXS patterns for the NiCo 35 wt% @MSU samples: as-synthesized and treated with UV for 30 min in different atmospheres.

The results of the XRD analysis are displayed in Figure 50. This analysis shows no substantial differences between the different atmospheres; the PBA intensity is clearly reduced, but no complete destruction can be observed.

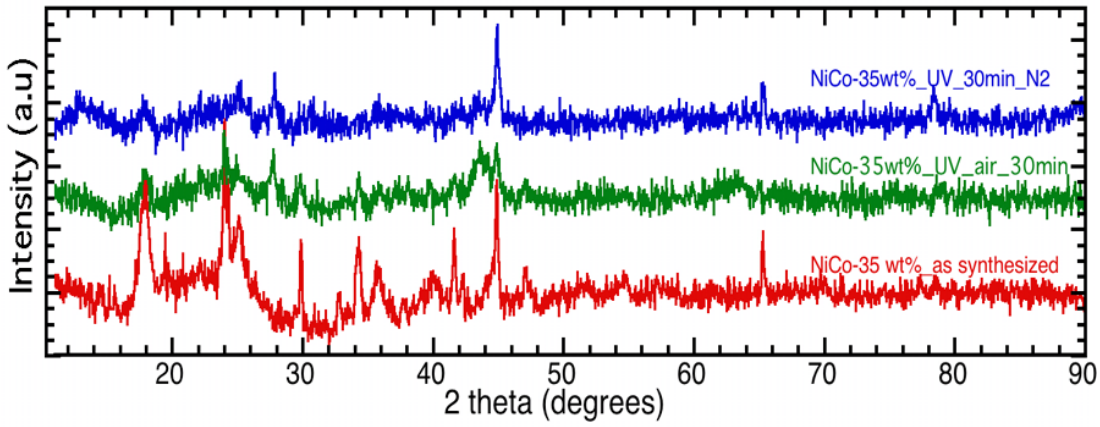

Figure 50. Diffraction patterns for the NiCo 35 wt% @MSU samples: as-synthesized and treated with UV for 30 min in different atmospheres.

Scherrer analysis of the first diffraction peak reveals the presence of 26 nm crystals in the as-synthesized sample, whereas the particle size is reduced to 11 nm when the sample is treated in nitrogen for 30 min.

The UV treatment was carried out using a 300 watt/inch microwave-powered electrodeless lamp model F300S with power supply model P300MT (Fusion UV Systems, INC®).

Chapter 6

Conclusion and Future Work

This work has examined, with respect to a number of systems, the effect of higher levels of PBAs on silica structure as well as on the final PBA product, Another main focus was the study under a variety of conditions of the impact of heat treatment on the structure of the materials obtained and on their magnetic properties. Compared to the conventional method, using MSU silica as a soft matrix for the confinement of the PBAs produced smaller and more uniform nanoparticles.

Still under investigation are the effects on the structure and magnetic properties of these materials when different treatments are used, such as UV and microwave irradiation.

Further investigation of the powder obtained is required with respect to the characterization of the magnetization at a variety of temperatures. It is known that in small particles, the spin-coating and annealing process can induce a large number of defects, causing a significant changes in the magnetic properties. Additional work could thus focus on making thin films of the previously studied Prussian blue analogues in order to determine their magnetic properties after a variety of thermal treatments have been applied.

Future work in this field should include an attempt to incorporate other Prussian blue analogues into a silica matrix, together with a determination of their properties. Of significant interest would be the development of the ability to synthesize SmCo and SmFe, whose very strong magnetic properties are already well known. Another possible project could then focus on the effect of UV and microwave treatment on these additional Prussian blue analogues.

While further work should be conducted before final success can be assured, the outcome of the research presented in this thesis can be seen as an excellent starting point for the preparation of magnetic materials that can be tailored and improved based on the use of different transition metals as well as the application of varied thermal treatments.

References

1. Spaldin, N., *Magnetic Materials fundamental and device application*. 2003.
2. Jiles, D., *Introduction to Magnetism and Magnetic Material*. Chapman and Hall: London, 1998; Vol. 2nd Ed.
3. Wuttig, M.; Yamada, N., Phase-change materials for rewriteable data storage. *Nature Materials* **2007,** *6* (12), 1004-1004.
4. M.Verdaguer, F. V., M.Verdaguer, F Villain, How molecules become magnetic (http:// obelix.physik.uni-bielefeld.de/~schnack/molmag/introduction.html).
5. Wernsdorfer, W., Classical and quantum magnetization reversal studied in nanometer-sized particles and clusters. *Advances in Chemical Physics, Vol 118* **2001,** *118*, 99-190.
6. LesliePelecky, D. L.; Rieke, R. D., Magnetic properties of nanostructured materials. **1996,** *8* (8), 1770-1783.
7. Néel, L. C. R., *Acad. Sci* **1949,** *228*, 664.
8. West, A. R., Basic solid state chemistry. **1999**.
9. Terris, B. D.; Thomson, T., Nanofabricated and self-assembled magnetic structures as data storage media. *Journal of Physics D-Applied Physics* **2005,** *38* (12), R199-R222.
10. B. D. Terris, T. T., *J. Phys. D: Appl. Phys* **2005,** *38*, R199–R222.
11. de Zarate, D. O.; Bouyer, F.; Zschiedrich, H.; Kooyman, P. J.; Trens, P.; Iapichella, J.; Durand, R.; Guillem, C.; Prouzet, E., Micromesoporous monolithic Al-MSU with a

widely variable content of aluminum leading to tunable acidity. *Chemistry of Materials* **2008,** *20* (4), 1410-1420.

12. Herrera, J. M.; Bachschmidt, A.; Villain, F.; Bleuzen, A.; Marvaud, V.; Wernsdorfer, W.; Verdaguer, M., Mixed valency and magnetism in cyanometallates and Prussian blue analogues. *Philosophical transactions. Series A, Mathematical, physical, and engineering sciences* **2008,** *366* (1862), 127-38.

13. Kahn, O., *Accounts of Chemical Research* **2000,** *33*, 647.

14. Verdaguer, M., Rational synthesis of molecular magnetic materials:a tribute to Olivier Kahn. *Polyhedron* **2001,** *20* (11-14), 1115-1128.

15. Kaye, S. S.; Long, J. R., Hydrogen storage in the dehydrated Prussian blue analogues M-3 Co(CN)(6) (2) (M = Mn, Fe, Co, Ni, Cu, Zn). *Journal of the American Chemical Society* **2005,** *127* (18), 6506-6507.

16. Dechambenoit, P.; Long, J. R., Microporous magnets. *Chemical Society Reviews* **2011,** *40* (6), 3249-3265.

17. Moriarty, P., Nanostructured materials. *Reports on Progress in Physics* **2001,** *64* (3), 297-381.

18. Heinrich, B., Magnetic nanostructures. From physical principles to spintronics. *Canadian Journal of Physics* **2000,** *78* (3), 161-199.

19. Buschow, K. H. J.; Naastepa.Pa; Westendo.Ff, PREPARATION OF SMCO5 PERMANENT MAGNETS. *Journal of Applied Physics* **1969,** *40* (10), 4029-&.

20. Matsushita, T.; Iwamoto, T.; Inokuchi, M.; Toshima, N., Novel ferromagnetic materials of SmCo5 nanoparticles in single-nanometer size: chemical syntheses and characterizations. *Nanotechnology* **2010,** *21* (9).

21. Larionova, J.; Guari, Y.; Sangregorio, C.; Guérin, C., Cyano-bridged coordination polymer nanoparticles. *New Journal of Chemistry* **2009,** *33* (6), 1177.

22. Mouawia, R.; Larionova, J.; Guari, Y.; Oh, S.; Cook, P.; Prouzet, E., Synthesis of Co3[Fe(CN)6]2 molecular-based nanomagnets in MSU mesoporous silica by integrative chemistry. *New Journal of Chemistry* **2009,** *33* (12), 2449.

23. Jonker, G. H.; Vansanten, J. H., FERROMAGNETIC COMPOUNDS OF MANGANESE WITH PEROVSKITE STRUCTURE. *Physica* **1950,** *16* (3), 337-349.

24. Strnat, K.; Hoffer, G.; Olson, J.; Ostertag, W.; Becker, J. J., A FAMILY OF NEW COBALT-BASE PERMANENT MAGNET MATERIALS. *Journal of Applied Physics* **1967,** *38* (3), 1001.

25. Liu, J. F.; Zhang, Y.; Hadjipanayis, G. C., High-temperature magnetic properties and microstructural analysis of Sm(Co,Fe,Cu,Zr), permanent magnets. *Journal of Magnetism and Magnetic Materials* **1999,** *202* (1), 69-76.

26. H.J. Fastenau, E. J. L., Aplication of rare earth permament magnets. *Journal of Magnetism and Magnetic Materials, 1570158* **1996,** *1-6*.

27. de Tacconi, N. R.; Rajeshwar, K.; Lezna, R. O., Metal hexacyanoferrates: Electrosynthesis, in situ characterization, and applications. *Chemistry of Materials* **2003,** *15* (16), 3046-3062.

28. Ng, C. W.; Ding, J.; Wang, L.; Gan, L. M.; Quek, C. H., Thermal-induced microstructural changes of nickel-iron cyanide. *Journal of Physical Chemistry A* **2000,** *104* (38), 8814-8822.

29. M. Verdaguer, G. S. G., *Magnetism, Mol. Mater* **2005,** *283*.

30. Vaucher, S.; Li, M.; Mann, S., Synthesis of Prussian blue nanoparticles and nanocrystal superlattices in reverse microemulsions. *Angewandte Chemie-International Edition* **2000,** *39* (10), 1793.

31. Catala, L.; Gloter, A.; Stephan, O.; Rogez, G.; Mallah, T., Superparamagnetic bimetallic cyanide-bridged coordination nanoparticles with T-B=9 K. *Chemical Communications* **2006,** (9), 1018-1020.

32. Shiba, F., Preparation of monodisperse Prussian blue nanoparticles via reduction process with citric acid. *Colloids and Surfaces a-Physicochemical and Engineering Aspects* **2010,** *366* (1-3), 178-182.

33. Pramanik, S.; Das, D.; Das, K.; Bhattacharya, S. C., Synthesis and characterization of nanodispersed molecular aggregates of Prussian Blue in Aerosol OT reverse micelle. *Journal of Nanoscience and Nanotechnology* **2007,** *7* (2), 663-667.

34. Johansson, A.; Widenkvist, E.; Lu, J.; Boman, M.; Jansson, U., Fabrication of high-aspect-ratio Prussian blue nanotubes using a porous alumina template. *Nano Letters* **2005,** *5* (8), 1603-1606.

35. Folch, B.; Guari, Y.; Larionova, J.; Luna, C.; Sangregorio, C.; Innocenti, C.; Caneschi, A.; Guérin, C., Synthesis and behaviour of size controlled cyano-bridged coordination

polymer nanoparticles within hybrid mesoporous silica. *New Journal of Chemistry* **2008,** *32* (2), 273.

36. Tiemann, M., Repeated templating. *Chemistry of Materials* **2008,** *20* (3), 961-971.

37. Mann, S.; Burkett, S. L.; Davis, S. A.; Fowler, C. E.; Mendelson, N. H.; Sims, S. D.; Walsh, D.; Whilton, N. T., Sol-gel synthesis of organized matter. *Chemistry of Materials* **1997,** *9* (11), 2300-2310.

38. Sanchez, C.; Rozes, L.; Ribot, F.; Laberty-Robert, C.; Grosso, D.; Sassoye, C.; Boissiere, C.; Nicole, L., "Chimie douce": A land of opportunities for the designed construction of functional inorganic and hybrid organic-inorganic nanomaterials. *Comptes Rendus Chimie* **2010,** *13* (1-2), 3-39.

39. Backov, R., Combining soft matter and soft chemistry: integrative chemistry towards designing novel and complex multiscale architectures. *Soft Matter* **2006,** *2* (6), 452-464.

40. Brinker, C. J., HYDROLYSIS AND CONDENSATION OF SILICATES - EFFECTS ON STRUCTURE. *Journal of Non-Crystalline Solids* **1988,** *100* (1-3), 31-50.

41. T. Yanagisawa, T. S., K. Kuroda, C. Kato., *Bull. Chem. Soc.Jpn* **1990,** *63*, 988.

42. Kresge, C. T.; Leonowicz, M. E.; Roth, W. J.; Vartuli, J. C.; Beck, J. S., ORDERED MESOPOROUS MOLECULAR-SIEVES SYNTHESIZED BY A LIQUID-CRYSTAL TEMPLATE MECHANISM. *Nature* **1992,** *359* (6397), 710-712.

43. D. Y. Zhao, J. L. F., Q. S. Huo, B. F. Chmwelka, G. D. Stucky,, *J Am. Chem. Soc* **1998,** *120*, 6024.

44. D. Y. Zhao, Q. S. H., J. L. Feng, B. F. Chmwelka, G. D. Stucky,, *J Am. Chem. Soc* **1998,** *120*, 6024.

45. J. V. Stark, K. K., *Chem. Mater* **1996,** *8*, 1913.

46. J. C. Yu, A. W. X., L. Z. Zhang, R. Q. Song, L. Wu, *J. Phys. Chem.B* **2004,** *108*, 64.

47. Bagshaw, S. A.; Prouzet, E.; Pinnavaia, T. J., TEMPLATING OF MESOPOROUS MOLECULAR-SIEVES BY NONIONIC POLYETHYLENE OXIDE SURFACTANTS. *Science* **1995,** *269* (5228), 1242-1244.

48. Prouzet, E.; Cot, F.; Nabias, G.; Larbot, A.; Kooyman, P.; Pinnavaia, T. J., Assembly of mesoporous silica molecular sieves based on nonionic ethoxylated sorbitan esters as structure directors. *Chem. Mater* **1999,** *11* (6), 1498-1503.

49. Wan, Y.; Zhao, D. Y., On the controllable soft-templating approach to mesoporous silicates. *Chemical Reviews* **2007,** *107* (7), 2821-2860.

50. Sjoblom, J., Stenius, P., Danielsson. J., Phase Equilibria of Nonionic Surfactants and the Formation of Microemulsions in Nonionic Surfactants. *phys. Chem. C* **1987,** *2*, 369-435.

51. Auvray, X.; Perche, T.; Petipas, C.; Anthore, R.; Marti, M. J.; Rico, I.; Lattes, A., Influence of Solvent-Headgroup Interactions on the Formation of Lyotropic Liquid Crystal Phases of Surfactants in Water and Nonaqueous Protic and Aprotic Solvents. *Langmuir* **1992,** *8*, 2671-2679.

52. Mouawia, R.; Larionova, J.; Guari, Y.; Oh, S.; Cook, P.; Prouzet, E., Synthesis of Co3[Fe(CN)6]2 molecular-based nanomagnets in MSU mesoporous silica by integrative chemistry. *New J. Chem.* **2009,** *33*, 2449-2456.

53. Shriver, D. F.; Brown, D. B., The Environment of Interstitial Ions in a Prussian Blue Analog, Co[Co(CN)6]2. *Inorg. Chem.* **1969,** *8* (1), 42-46.

54. Buser, H. J.; Schwarzenbach, D.; Petter, W.; Ludi, A., The Crystal Structure of Prussian Blue: Fe4[Fe(CN)6]3·xH2O. *Inorg. Chem.* **1977,** *16* (11), 2704-2710.

55. Cao, M.; Wu, X.; He, X.; Hu, C., Shape-controlled synthesis of Prussian blue analogue Co3[Co(CN)6]2 nanocrystals. *Chem Commun* **2005,** (17), 2241-3.

56. Daniel H. M. Buchold, C. F., Synthesis of Nanoscale Co3[Co(CN)6]2 in Reverse Microemulsions. *Chem. Mater* **2007,** *19*, 3376-3380.

57. Zhou, H. S.; Kundu, D.; Honma, I., Synthesis of oriented meso-structure silica functional thin film. *Journal of the European Ceramic Society* **1999,** *19* (6-7), 1361-1364.

58. Han, S.; Hou, W.; Huang, X.; Zheng, L.; Wang, Y., Effect of concentration of nitric acid on transition of mesoporous silica structure. In *Recent Progress in Mesostructured Materials, Proceedings of the 5th International Mesostructured Materials Symposium - Imms2006*, 2007; Vol. 165, pp 101-104.

59. Asamoto, M.; Yahiro, H., Catalytic Property of Perovskite-Type Oxide Prepared by Thermal Decomposition of Heteronuclear Complex. *Catalysis Surveys from Asia* **2009,** *13* (4), 221-228.

60. Asamoto, M.; Iwasaki, Y.; Yamaguchi, S.; Yahiro, H., Synthesis of perovsite-type oxide catalysts, Ln(Fe, Co) (Ln = La, Pr, Sm, Gd, Dy, Ho, Er, and Yb), from the thermal decomposition of the corresponding cyano complexes. *Catalysis Today* **2012,** *185* (1), 230-235.

61. Sun, H. L.; Shi, H. T.; Zhao, F.; Qi, L. M.; Gao, S., Shape-dependent magnetic properties of low-dimensional nanoscale Prussian blue (PB) analogue SmFe(CN)(6). 4H(2)O. *Chemical Communications* **2005,** (34), 4339-4341.

62. Zhou, X.; Wong, W.-T.; Faucher, M. D.; Tanner, P. A., Crystallographic and infrared spectroscopic study of bond distances in Ln[Fe(CN)6]·4H2O (Ln=lanthanide). *Journal of Solid State Chemistry* **2008,** *181* (11), 3057-3064.

63. Mami, Y.; Shin-ya, Y., Nanometric Metal-Organic Framework of Ln[Fe(CN)6]: Morphological Analysis and Thermal Conversion Dynamics by Direct TEM Observation. *phys. Chem. C* **2009,** *113*, 21531-21537.

64. Mohseni Meybodi, S.; Hosseini, S. A.; Rezaee, M.; Sadrnezhaad, S. K.; Mohammadyani, D., Synthesis of wide band gap nanocrystalline NiO powder via a sonochemical method. *Ultrasonics Sonochem.* **2012,** *19* (4), 841-5.

65. Verma, S.; Joshi, H. M.; Jagadale, T.; Chawla, A.; Chandra, R.; Ogale, S., Nearly monodispersed multifunctional NiCo2O4 spinel nanoparticles: Magnetism, infrared transparency, and radiofrequency absorption. *J. Phys. Chem. C* **2008,** *112* (39), 15106-15112.

66. L. Néel, C. D., B. Dreyfus, P.D. de Gennes, Editors *Low Temperature Physics, Gordon and Beach, New York* **1962**, 413.

67. Kim, J. G.; Pugmire, D. L.; Battaglia, D.; Langell, M. A., Analysis of the NiCo2O4 spinel surface with Auger and X-ray photoelectron spectroscopy. *Applied Surface Science* **2000,** *165* (1), 70-84.

68. Kodama, R. H.; Makhlouf, S. A.; Berkowitz, A. E., Finite size effects in antiferromagnetic NiO nanoparticles. *Physical Review Letters* **1997,** *79* (7), 1393-1396.

69. Binder, K.; Young, A. P., SPIN-GLASSES - EXPERIMENTAL FACTS, THEORETICAL CONCEPTS, AND OPEN QUESTIONS. *Reviews of Modern Physics* **1986,** *58* (4), 801-976.

70. Garcia, J. L.; Lopez, A.; Lazaro, F. J.; Martinez, C.; Corma, A., Iron oxide particles in large pore zeolites. *Journal of Magnetism and Magnetic Materials* **1996,** *157*, 272-273.

71. Cabo, M.; Pellicer, E.; Rossinyol, E.; Castel, O.; Surinach, S.; Baro, M. D., Mesoporous NiCo2O4 Spinel: Influence of Calcination Temperature over Phase Purity and Thermal Stability. *Crystal Growth & Design* **2009,** *9* (11), 4814-4821.

72. Nogues, J.; Sort, J.; Langlais, V.; Skumryev, V.; Surinach, S.; Munoz, J. S.; Baro, M. D., Exchange bias in nanostructures. *Physics Reports-Review Section of Physics Letters* **2005,** *422* (3), 65-117.

73. Cheng, M.; Wen, M.; Zhou, S.; Wu, Q.; Sun, B., Solvothermal Synthesis of NiCo Alloy Icosahedral Nanocrystals. *Inorg. Chem.* **2012,** *51* (3), 1495-1500.

74. Wang, Y. Q.; Yang, C. M.; Schmidt, W.; Spliethoff, B.; Bill, E.; Schuth, F., Weakly ferromagnetic ordered mesoporous CO(3)O(4) synthesized by nanocasting from vinyl-functionalized cubic Ia3d mesoporous silica. *Advanced Materials* **2005,** *17* (1), 53-+.

75. Kundig, W.; Kobelt, M.; Appel, H.; Constaba.G; Lindquis.Rh, MOSSBAUER STUDIES OF C03O4 - BULK MATERIAL AND ULTRAFINE PARTICLES. *Journal of Physics and Chemistry of Solids* **1969,** *30* (4), 819-&.

76. Serrano, A.; Pinel, E. F.; Quesada, A.; Lorite, I.; Plaza, M.; Perez, L.; Jimenez-Villacorta, F.; de la Venta, J.; Martin-Gonzalez, M. S.; Costa-Kramer, J. L.; Fernandez, J. F.; Llopis, J.; Garcia, M. A., Room-temperature ferromagnetism in the mixtures of the TiO2 and Co3O4 powders. *Physical Review B* **2009,** *79* (14).

77. Fu, W.; Yang, H.; Hari, B.; Liu, S.; Li, M.; Zou, G., Preparation and characteristics of core-shell structure cobalt/silica nanoparticles. *Materials Chemistry and Physics* **2006,** *100* (2-3), 246-250.

78. Fernandez, C. D.; Mattei, G.; Sangregorio, C.; Battaglin, C.; Gatteschi, D.; Mazzoldi, P., Superparamagnetism and coercivity in HCP-Co nanoparticles dispersed in silica matrix. *Journal of Magnetism and Magnetic Materials* **2004,** *272*, E1235-E1236.

79. Lu, N.; Song, X.; Zhang, J., Crystal structure and magnetic properties of ultrafine nanocrystalline SmCo3 compound. *Nanotechnology* **2010,** *21* (11).

80. Chakka, V. M.; Altuncevahir, B.; Jin, Z. Q.; Li, Y.; Liu, J. P., Magnetic nanoparticles produced by surfactant-assisted ball milling. *Journal of Applied Physics* **2006,** *99* (8).

81. Kappe, C. O., Microwave dielectric heating in synthetic organic chemistry. *Chemical Society Reviews* **2008,** *37* (6), 1127-1139.

82. Vondrova, M.; Burgess, C. M.; Bocarsly, A. B., Cyanogel coordination polymers as precursors to transition metal alloys and intermetallics - from traditional heating to microwave processing. *Chemistry of Materials* **2007,** *19* (9), 2203-2212.